# Transformer-based spatial-temporal detection of apoptotic cell death in live-cell imaging.

**Alain Pulfer[1,2,&], Diego Ulisse Pizzagalli[1,3,&], Paolo Armando Gagliardi[4,&], Lucien Hinderling[4], Paul Lopez[5], Romaniya Zayats[5], Pau Carrillo-Barberà[1,6], Paola Antonello[1,4], Miguel Palomino-Segura[7], Alessandro Giusti[8], Marcus Thelen[1], Luca Maria Gambardella[8], Thomas T. Murooka[5], Olivier Pertz[4], Rolf Krause[3], Santiago Fernandez Gonzalez[1,*]**

[1] Institute for Research in Biomedicine, Faculty of Biomedical Sciences, USI—Switzerland

[2] Department of Information Technology and Electrical Engineering, ETH Zurich—Switzerland

[3] Euler Institute, USI—Switzerland

[4] Institute of Cell Biology, University of Bern—Switzerland

[5] University of Manitoba, Winnipeg—Canada

[6] Instituto de Biotecnología y Biomedicina (BioTecMed), Universitat de València—Spain.

[7] Centro Nacional de Investigaciones Cardiovasculares—Spain

[8] Dalle Molle Institute for Artificial Intelligence, IDSIA—Switzerland

**[&] Contributed equally**

**[*] Corresponding author santiago.gonzalez@irb.usi.ch**

## Abstract

Intravital microscopy has revolutionized live cell imaging by allowing the study of spatial-temporal cell dynamics in living animals. However, the complexity of the data generated by this technology has limited the development of effective computational tools to identify and quantify cell processes. Amongst them, apoptosis is a crucial form of regulated cell death involved in tissue homeostasis and host defense. Live-cell imaging enabled the study of apoptosis at the cellular level, enhancing our understanding of its spatial-temporal regulation. However, at present, no computational method can deliver label-free detection of apoptosis in microscopy time-lapses. To overcome this limitation, we developed ADeS, a deep learning-based apoptosis detection system that employs the principle of activity recognition. We trained ADeS on extensive datasets containing more than 10,000 apoptotic instances collected both *in vitro* and *in vivo*, achieving a classification accuracy above 98% and outperforming state-of-the-art solutions. ADeS is the first method capable of detecting the location and duration of multiple apoptotic events in full microscopy time-lapses, surpassing human performance in the same task. We demonstrated the effectiveness and robustness of ADeS across various imaging modalities, cell types, and staining techniques. Finally, we employed ADeS to quantify cell survival *in vitro* and tissue damage *in vivo*, demonstrating its potential application in toxicity assays, treatment evaluation, and inflammatory dynamics. Our findings suggest that ADeS is a valuable tool for the accurate detection and

38  quantification of apoptosis in live-cell imaging and, in particular, intravital microscopy data, providing

39  insights into the complex spatial-temporal regulation of this process.

40

41

42  **Keywords:** *Apoptosis; Deep Learning, Transformers, Cell death, Intravital 2-photon microscopy;*

43  *Bioimaging Analysis; Artificial Intelligence; Activity Recognition; Computer Vision; Spatial-temporal*

44  *Dinamics.*

45

## 46  1. Introduction

47

48  In the last two decades, Intravital microscopy (IVM) has revolutionized live-cell imaging by enabling

49  microscopy acquisitions *in situ* across different organs, making it one of the most accurate model to

50  describe cellular activities within a living host(Sumen et al. 2004). In particular, multiphoton intravital

51  microscopy (MP-IVM) generates in-depth 3D data that encompass multiple channels for up to several

52  hours of acquisition (x,y,z + t)(Secklehner, Celso, and Carlin 2017; Helmchen and Denk 2005;

53  Rocheleau and Piston 2003), thus providing unprecedented insights into cellular dynamics and

54  interactions(Pizzagalli et al., n.d.). The resulting MP-IVM data stream is a complex and invaluable

55  source of information, contributing to enhance our understanding of several fundamental

56  processes(Beltman et al. 2009; Sumen et al. 2004).

57

58  Apoptosis is a form of regulated cell death(D'Arcy 2019; D. Tang et al. 2019) which plays a crucial role

59  in several biological functions, including tissue homeostasis, host protection, and immune

60  response(Opferman 2008). This process relies on the proteolytic activation of caspase-3-like

61  effectors(Shalini et al. 2015), which yields successive morphological changes that include cell

62  shrinkage, chromatin condensation, DNA fragmentation, membrane blebbing(Galluzzi et al. 2018;

63  Elmore 2007; Saraste and Pulkki 2000), and finally, apoptotic bodies formation(Coleman et al. 2001).

64  Due to its crucial role, dysregulations of apoptosis can lead to severe pathological conditions, including

65  cronic inflammatory diseases and cancer(Hotchkiss and Nicholson 2006; Fesik 2005). Consequently,

66  precise tools to identify and quantify apoptosis in different tissues are pivotal to gain insights on this

67  mechanism and its implications at the organism level.

68

69  Traditional techniques to quantify apoptosis rely on cellular staining on fixed cultures and tissues(Loo

70  2011; Kyrylkova et al. 2012; Atale et al. 2014; Vermes et al. 1995; Sun et al. 2008) or flow

71  cytometry(Darzynkiewicz, Galkowski, and Zhao 2008; Vermes et al. 1995). However, these methods

72  do not allow the temporal characterization of the apoptotic process. Moreover, they potentially introduce

73  artifacts caused by sample fixation(Schnell et al. 2012). Live-cell imaging can overcome these limitation

74  by unraveling the dynamic aspects of apoptosis with the aid of fluorescent reporters, such as Annexin

75  staining(Atale et al. 2014) or the activation of Caspases(Takemoto et al. 2003). However, the use of

76  biochemical reporters *in vivo* could potentially interfere with physiological functions or lead to cell

77  toxicity(Jensen 2012). For these reasons, label-free detection of apoptosis represent a critical
78  advancement in the field of cell death.

79

80  Computational methods could address this need by automatically detecting individual apoptotic cells
81  with high spatial and temporal accuracy. In this matter, deep learning (DL) and activity recognition (AR)
82  could provide a playground for the classification and detection of apoptosis based on morphological
83  features(Poppe 2010). Accordingly, recent studies showed promising results regarding the
84  classification of static frames(Kranich et al. 2020; Verduijn et al. 2021) or time-lapses(Mobiny et al.
85  2020) portraying single apopotic cells. However, none of the available methods can apply for the
86  detection of apoptosis in microscopy movies depicting multiple cells. Therefore we developed ADeS, a
87  novel apoptosis detection system which employs a transformer DL architecture and computes the
88  location and duration of multiple apoptotic events in live-cell imaging. Here we show that our
89  architecture outperforms state-of-the-art DL techniques and efficiently detects apoptotic events in a
90  broad range of imaging modalities, cellular staining, and cell types.

91

## 92  2. Results

93  **2.1. An *in vitro* and *in vivo* live-cell imaging data.** Curated and high-quality datasets containing
94  numerous instances of training samples are critical for developing data-hungry methods such as
95  supervised DL algorithms(Adadi 2021). To this end, we generated two distinct datasets encompassing
96  epithelial cells (*in vitro*) and leukocytes (*in vivo*) undergoing apoptotic cell death. In addition, the two
97  datasets include different imaging modalities (confocal and intravital 2-photon), biological models, and
98  training-set dimensionalities. A meaningful difference between the datasets pertains to the staining
99  methods and the morphological hallmarks, which define the apoptotic process in both models. In the *in*
100 *vitro* model, the expression of nuclear markers allowed us to observe apoptotic features such as
101 chromatin condensation and nuclear shrinkage(Saraste and Pulkki 2000), whereas in the *in vivo* model,
102 cytoplasmic and membrane staining highlighted morphological changes such as membrane blebbing
103 and the formation of apoptotic bodies(Saraste and Pulkki 2000). Accordingly, we have manually
104 annotated these datasets based on the presence of the specific hallmarks, ensuring that each dataset
105 includes two class labels depicting either apoptotic or non-apoptotic cells. These two datasets constitute
106 the first step toward creating, testing, and validating our proposed apoptosis detection routine.

107

108 To generate the *in vitro* dataset we used epithelial cells because, among the human tissues, they have
109 the highest cellular turnover driven by apoptosis(Van Der Flier and Clevers 2009). Nevertheless, from
110 the bioimaging perspective, the epithelium is a densely packed tissue with almost no extracellular
111 matrix, making it extremely challenging to analyze. As such, in epithelial research, there is a pressing
112 need for computational tools to identify apoptotic events automatically. To this end, we imaged and
113 annotated the human mammary epithelial cells expressing a nuclear fluorescent marker (Fig.1A),
114 obtaining 13120 apoptotic nuclei and 301630 non apoptotic nuclei image sequences (Fig. 1B-C,
115 Supplementary 1A). Nuclear shrinkage and chromatin condensation, two of the most prototypical
116 hallmarks of apoptosis (Fig. 1C), formed our criteria for manual annotation. We confirmed that non-

3

117   apoptotic nuclei had constant area and chromatin density from the generated time-lapses. In contrast,

118   apoptotic nuclei underwent a decrease in area and an increase in chromatin condensation (Fig. 1D).

119   The resulting dataset captured the heterogeneity of apoptotic cells in epithelial tissue, including early

120   nuclear fragmentation, a rapid shift along the x and y axes, and extrusion through the z dimension

121   (Supplementary Fig. 1B–C). Moreover, our dataset incorporates the typical difficulties of automatically

122   annotating apoptotic events from live microscopy of a densely packed tissue (Supplementary Fig. 1D)

123   with the accumulation of apoptotic bodies (Supplementary Fig. 1E) and across multiple microscope

124   hardware settings (Supplementary Fig. 1F).

125

126   To generate an *in vivo* dataset, we focused on polymorphonucleated leukocytes (neutrophils and

127   eosinophils) that expressed a fluorescent marker. In these early immune responders, apoptosis is a

128   crucial process that orchestrates their disposal, consequently determining the duration of the

129   inflammation(Fox et al. 2010). To acquire instances of apoptotic leukocytes, we performed MP-IVM in

130   anesthetized mice by surgically exposing either the spleen or the popliteal lymph node (Fig. 1E-F). The

131   resulting time-lapses (Fig. 1G) provided 3D imaging data encompassing consecutive multi-focal planes

132   (3D) and multiple imaging channels. Then, from the generated MP-IVM movies, we generated cropped

133   sequences of fixed size that tracked apoptotic cells for the duration of their morphological changes

134   (59x59 pixels + time; Fig. 1H-I). This procedure was applied to 30 MP-IVM movies, generating 120

135   apoptotic sequences (supplementary Fig. 1G). Furthermore, we annotated random instances of non-

136   apoptotic events, generating 535 cropped samples. To characterize the heterogeneity of the movies,

137   we manually quantified the cell number per field of view (87 ± 76), the shortest distance between cells

138   (21.2 $\mu$M ± 15.4), and the signal-to-noise ratio (8.9 ± 3.6; supplementary Fig. 1 H–J). We assumed that

139   the morphological changes associated with apoptosis occur within defined time windows for detection

140   purposes. Hence, we estimated the median duration of the morphological changes corresponding to 8

141   frames (supplementary Fig. 1K–L, respectively). In addition, to classify apoptotic cells within defined

142   spatial regions, we considered them to be non-motile. This assumption was confirmed when we found

143   that apoptotic cells exhibited a displacement and speed that were not significantly different from those

144   of arrested cells (supplementary Fig. 1M).

145

146   **2.2. ADeS, a pipeline for apoptosis detection.** Detecting apoptosis in live-cell imaging is a two-step

147   process involving the correct detection of apoptotic cells in the movies (x,y) and the correct estimation

148   of the apoptotic duration (*t*). To fulfill these requirements, we designed ADeS as a set of independent

149   modules assigned to distinct computational tasks (Fig. 2). As an input, ADeS receives a 2D

150   representation of the microscopy acquisitions (Fig. 2A) obtained from the normalization of 2D raw data

151   or the maximum projection of 3D data(Shi et al. 2015). This processing step ensures the standardization

152   of the input, which might differ in bit depth or acquisition volume. After that, we employ a selective

153   search algorithm(Girshick 2015; Uijlings et al. 2013) to compute regions of interest (ROIs) that might

154   contain apoptotic cells (Fig. 2B). For each ROI at time (*t*), ADeS extracts a temporal sequence of *n*

155   frames ranging *from t - n*/2 to *t + n*/2 (Fig. 2C). The resulting ROI sequence is standardized in length

156   and passed to a DL classifier (Fig. 3), which determines whether it is apoptotic or non-apoptotic. Finally,

157    each apoptotic sequence is depicted as a set of bounding boxes and associated probabilities (Fig. 2D)

158    generated from the predicted trajectories (x, y, t, ID; Fig. 2E). From this readout, ADeS can generate a

159    heatmap representing the likelihood of apoptotic events throughout a movie (Fig. 2F, left), together with

160    a cumulative sum of the predicted cell deaths (Fig. 2F, right).

161

162    For the classification of apoptotic sequences, we proposed a Conv-Transformer architecture (Fig. 3). In

163    the proposed architecture, a convolutional module extracts the spatial features of the apoptotic cells,

164    whereas attention-based nlocks evaluates the temporal relationship between consecutive frames.

165

166    **2.3. Training and deployment *in vitro*.** As previously described, ADeS is a multiple-block pipeline,

167    and its application and validation to detect apoptotic cells in live-cell imaging follow two main steps: (1)

168    the training of the DL classifier with a target dataset and (2) its deployment on live-cell imaging

169    acquisitions. As opposed to *in vivo* acquisitions, *in vitro* time-lapses are more homogeneous in their

170    content and quality, thus representing the first dataset in order of complexity for the training of ADeS.

171    For this reason, we formulated the learning problem as a binary classification task that assigned non-

172    apoptotic sequences to the class label 0 and apoptotic sequences to the class label 1 (Supplementary

173    Fig. 2A). The class label 0 included instances of healthy nuclei and nuclei undergoing mitotic division

174    (which can resemble apoptotic events).

175

176    Successively, to validate the proposed Conv-Transformer architecture for apoptosis classification, we

177    compared it with the performances of a CNN, a 3DCNN, and a Conv-LSTM. To this end, the four models

178    were trained on a dataset containing 13.120 apoptotic and 13.120 non-apoptotic events, using a 0.12

179    validation split (Table 1). Results show that the frame accuracy of the CNN is low, possibly due to

180    morphological heterogeneity over consecutive frames, and therefore unsuitable for the task. By

181    contrast, the 3DCNN and the Conv-LSTM displayed high sequence accuracy, F1 score and AUC,

182    confirming that the temporal information within frames is pivotal to correctly classifying image

183    sequences containing apoptotic cells. Nonetheless, the proposed Conv-Transformer outperformed both

184    the 3DCNN and the Conv-LSTM, establishing itself as the final DL architecture at the chore of ADeS.

185

186    Successively, we deployed a preliminary trained network on control movies withouth apoptotic events

187    to collect false positives that we used to populate the class label 0, thus ensuring a systematic decrease

188    in the misclassification rate (Supplementary Fig. 2B). Using the latter generated dataset, we trained the

189    Conv-Transformer for 100 epochs using an unbalanced training set with a 1:10 ratio of apoptotic to non

190    apoptotic cells (Fig. 4A). After deploying the trained model on 1000 testing samples, the confusion

191    matrix (Fig. 4B) displayed a scant misclassification rate (2.68%), similarly distributed between false

192    positives (1.04%) and false negatives (1.64%). Accordingly, the receiver operating characteristic (ROC)

193    of the model skewed to the left (AUC = 0.99, Fig. 4C). This skew indicates a highly favorable tradeoff

194    between the true positive rate (TPR) and false positive rate (FPR), which the overall predictive accuracy

195    of 97.32% previously suggested (Fig. 4B). Altogether, these metrics suggest an unprecedented

196    accuracy of the DL model in the classification of apoptotic and non-apoptotic sequences. However, they

5

197  only reflect the theoretical performances of the classifier applied to cropped sequences depicting a
198  single cell at a time.

199

200  To validate ADeS on full-length microscopy acquisitions, we deployed it on six testing movies that were
201  not part of the training set. Each testing movie had been annotated manually and contained a variable
202  number of ground-truth apoptosis (98 ± 21) and a comparable cell density (1705 ± 124). Moreover, all
203  movies had identical magnification (20x), duration (21 h), and sampling rate (5 min). In order to test
204  ADeS on these movies, we adopted an unbiased approach and we did not hard-tune the hyper-
205  parameters of the model (see Material and Methods), specifying only a stringent confidence threshold
206  (0.995) and a temporal window based on the average duration of the nuclear hallmarks (9 frames). As
207  a result, ADeS could predict the location and timing of the apoptotic nuclei (Fig. 4D, Supplementary
208  Movie 1), enabling the detection of multiple apoptoses in a densely packed field of view (Fig. 4E–F). To
209  quantify these performances, we compared the prediction of ADeS to the annotated ground truths
210  (x,y,t). By doing this, we found that the average TPR, or sensitivity, was 82.01% (ranging from 77% to
211  92%), while the average FPR was 5.95% (Fig. 4G). The undetected apoptotic events were likely a
212  consequence of the heterogeneity of nuclear fragmentation, which can vastly differ in signal intensity,
213  size, focal plane, and duration (Supplementary Fig.1). Nonetheless, hard tuning the model could further
214  increase the sensitivity without additional training data, such as by adjusting the temporal interval or by
215  lowering the confidence threshold. With respect to the false positives, most were mitotic cells, due to
216  their morphological similarities with aoptotic nuclei. Nevertheless, the FPR was contained, translating
217  into a new false positive every 4 frames (or 20 minutes of acquisition). This rate confirmed that ADeS
218  is overall robust, especially in light of movies depicting 1700 cells per frame.

219

220  Concerning the spatial-temporal dynamics, the apoptotic count over time highlighted a tight relationship
221  between ground truth apoptosis and correct detections of ADeS (Fig. 4H). Accordingly, the two curves
222  were divergent but highly correlative (Pearson r = 0.998), proving that ADeS can successfully capture
223  cell death dynamics. A 2D scatterplot (x, y, t = radius; Fig. 4I) visually depicted the spatial-temporal
224  proximity between ADeS and the ground truth, indicating overlap between the two scatter populations.
225  Nearest neighbor (NN) analysis further captureed this relationship; the average distance between all
226  ADeS predictions (true positives + false positives) and the NN in the ground truth was 30 pixels. In
227  contrast, randomly generated predictions had a ground truth NN within a 52-pixel radius (Fig. 4J).
228  Considering instead the true positives only, we observed that they were in close spatial proximity to the
229  ground truth, with most predictions falling within a 20-pixel radius (Fig. 4K). The difference between the
230  predicted timing of apoptosis and the one annotated in the ground truth was also slight, with an average
231  discard of 3.46 frames (Fig. 4L). Interestingly, ADeS showed a bias toward late detections, which is
232  explained considering that operators annotated the beginning of the apoptosis, whereas ADeS learned
233  to detect nuclear disruption, occurring at the end of the process. Altogether, these quantifications
234  indicate that ADeS detects apoptotic nuclei with high spatial and temporal accuracy, establishing a
235  novel comparative baseline for this task.

236

**2.4. 3D rotation of the *in vivo* dataset.** Upon the successful application of ADeS *in vitro*, the next step in complexity was detecting apoptosis *in vivo* time lapses. The latter is inherently more challenging due to different factors, including high background signal, autofluorescence, and the presence of collagen(Pizzagalli et al. 2018), among others. For this purpose, we re-trained ADeS using the *in vivo* data described in Figure 1. However, one of the main limitations of supervised DL is the need for large datasets, and the finite number of MP-IVM acquisitions and apoptotic instances represented a bottleneck for the training of ADeS. To overcome this limitation, we implemented a custom data augmentation strategy that exploits 3D volumetric rotations, as previously performed in other studies (Zhuang et al. 2019; Xu, Li, and Zhu 2020). Accordingly, each 3D apoptotic sequence underwent multiple spatial rotations and was successively projected in 2D (Fig. 5A). This procedure enabled us to increase the dataset of a 100 fold factor withouth introducing imaging artifacts, as each volume rotation was a physiological representation of the cell (Fig. 5B).

**2.5. Training and deployment *in vivo*.** To train ADeS using the latter rotated *in vivo* dataset, we defined a binary classification task in which ROIs containing apoptotic cells were assigned to the class label 1. In contrast, all remaining ROIs, including healthy cells and background elements, were assigned to the class label 0 (Supplementary Fig. 3A). Subsequently, we trained the DL classifier for 200 epochs. Finally, we performed 5-fold cross-validation according to the ID of the movies (Fig. 6A). The resulting confusion matrix demonstrated a classification accuracy of 97.80% and a 2.20% missclassification rate that is primarily due to type II error (1.80% false negatives) (Fig. 6B). Analogous to the tests *in vitro*, classification *in vivo* proved highly effective in predicting apoptotic and non-apoptotic instances. The ROC of the model, which indicated high sensitivity and a low FPR, supported this favorable result (Fig. 6C).

We then benchmarked ADeS in the detection task performed on a set of 23 MP-IVM acquisitions of immune cells undergoing apoptosis. Unlike *in vitro* settings, *in vivo* acquisitions displayed high variability in cell number, auto-fluorescence, signal intensity, and noise levels (Supplementary Fig. 3B). Still, ADeS correctly predicted the location and timing of cells undergoing apoptosis (Fig. 6H, Supplementary Movie 2), indicating its robustness to increasingly populated fields of view (Supplementary Fig. 3C). In addition, we successfully applied the pipeline to neutrophils imaged in the lymph node (Fig. 6D) and eosinophils in the spleen (Fig. 6E). By comparing ADeS predictions with the annotated ground truths, we found that our pipeline detected apoptotic events with a TPR of 81.3% and an FPR of 3.65% (Fig. 6F). The detections, provided in the form of bounding boxes and trajectories, indicated the coordinates and duration of the events. Hence, to measure how close they were to the annotated trajectories, we employed the tracking accuracy metric (TRA), a compound measure that evaluates the similarities between predicted and ground truth trajectories. The average TRA was above 0.9, indicating the high fidelity of the trajectories predicted by ADeS (Fig. 6G).

Next, we compared ADeS to human annotation performed by three operators on five testing movies. As a result, ADeS displayed an upward trend of the TPR and a downward trend of the FPR. However, we found no significant difference in the TPR and FPR (Fig. 6H). Regardless, ADeS performances

7

275   appeared to be distributed across two distinct groups: a large group with an average sensitivity of 100%
276   and a smaller group with an average sensitivity of 53% (Fig. 6H). To understand this discrepancy, we
277   applied hierarchical clustering to the testing videos according to their imaging properties and biological
278   content (Fig. 6I), thus generating two major dendrograms. The first dendrogram mostly contained videos
279   with reduced sensitivity (yellow) and was defined by a high cell number, high noise levels, short cell
280   distance, and a saturated and fluctuating image signal. Most notably, the cell number played a crucial
281   role in overall performance, as reflected in the fact that an increment of this parameter resulted in a
282   pronounced decrease in the TPR and a moderate increase in the FPR (Fig. 6J). Incidentally, the positive
283   predictive value (PPV) was significantly lower in videos with poor SNR and, although not statistically
284   significant, the PPV was lower when the signal standard deviation was higher (Fig. 6K). Following these
285   observations, we hypothesized that the quality of a movie predicts ADeS performance. Hence, we
286   combined the parameters highlighted by the clustering analysis (Fig. 6I) into a single score ranging from
287   zero to one (one indicating the highest and ideal score) and, in doing so, found there to be a weak
288   correlation between the video quality and the sensitivity of ADeS (Fig. 6L). However, this trend was
289   evident only when we considered videos with suboptimal sensitivity; indeed, in these cases, we found
290   a strong correlation (0.72), confirming that the video quality partially explains the observed
291   performances (Fig. 6M).

293   Finally, we evaluated how the biological variability *in vivo* could affect the readout of ADeS, defining
294   nine distinct biological categories, including apoptotic cells, healthy cells, and background elements.
295   For all biological categories, the classification accuracy was above 80%, except for overlapping cells
296   and cells with high membrane plasticity (Supplementary Fig. 3D).

298   **2.6. Comparison with the state-of-the-art.** To compare the performance of ADeS with other state-of-
299   the-art algorithms for cell death quantification, we conducted a comprehensive literature review. For
300   each study, we reported the attained classification accuracy, the experimental setup, the architecture
301   of the classifier, the capability of detecting cell death events in movies, and the number of cell deaths
302   in the training set (Table 2). Initial results indicate that ADeS achieved the highest classification
303   accuracy, but a direct comparison in terms of accuracy is not meaningful due to the differences in
304   datasets, including distinct cell types, different types of cell death, and varying dataset sizes. For a more
305   appropriate benchmark, we refer to Table 1, which shows that our classifier outperformed the baseline
306   re-implementations of the main classifiers used in other studies.

308   From Table 2, we observe that ADeS is the only algorithm for cell death quantification that has been
309   applied *in vivo*. Additionally, only ADeS and the study by Vicar and colleagues(Vicar et al. 2020)
310   effectively detected apoptotic cells in fully uncropped microscopy movies, which is a significant
311   achievement given the computational challenge associated with the task. However, Vicary and
312   colleagues relied on the temporal analysis of cell trajectories, while ADeS used vision-based methods
313   to directly analyze consecutive frames of a movie. As a result, ADeS offers a comprehensive and

314 pioneering pipeline for effectively applying vision-based classifiers to detect cell death in imaging time-
315 lapses.

316

317 **2.7. Applications for toxicity assay *in vitro*.** A common application of cell death staining is the
318 evaluation of the toxicity associated with different compounds(Schmid, Uittenbogaart, and Jamieson
319 2007; Atale et al. 2014) or the efficacy of an apoptotic-inducing treatment. Here, we show that ADeS
320 has analogous purposes and can effectively quantify the toxicity of different compounds *in vitro*. For
321 this application, we grew epithelial cells *in vitro*, treating them with PBS and three increasing
322 concentrations of doxorubicin, a chemotherapeutic drug that elicits apoptosis in the epithelium(Eom et
323 al. 2005). Epithelial cells were seeded with the same density of cells per well, and all four conditions
324 had the same confluence before the treatment. However, at 24 h. post-acquisition, the number of
325 survivor cells was inversely proportional to the doxorubicin concentration (Fig. 7A). We confirmed this
326 trend using ADeS (Supplementary Movies 3–6), which measured the lowest mortality after 24 h. in PBS
327 (62 cells), followed by doxorubicin concentrations of 1.25 µM (95 cells), 2.50 µM (167 cells), and 5.00
328 µM (289 cells). Moreover, ADeS predicted distinct pharmacodynamics (Fig. 7B), which can define the
329 drug concentration and experimental duration required to reach a specific effect in the apoptotic count.
330 To this end, each time point in Figure 7B also defines a dose-response relationship. Here we provide
331 two dose-responses curves at 5 h. and 24 h. post-treatment, showing different pharmacodynamics
332 (EC50 5h = 2.35, Hill slope 5h = 3.81, EC50 24h = 4.47, Hill slope 24h = 1.93, Fig. 7C–D). Notably, the
333 fit can project the dose-responses for higher drug concentrations, predicting the maximum effect size
334 at a given time. For instance, at 24 h. post treatment, a 10 µM titration attains 86% of the maximum
335 effect (456 apoptotic cells), whereas a further increase in the concentration of the drug leads only to a
336 moderate increase of the toxicity (Fig. 7E). We argue that this approach helps to maximize the effect of
337 a drug on a designated target, while minimizing collateral damage done to non-target cells. For instance,
338 in chemotherapies employing doxorubicin, apoptosis of epithelial cells is an undesired effect. Therefore,
339 researchers can select a titration of the drug and a duration of the treatment that does not affect the
340 epithelium yet still positively affects the tumor. Finally, we also demonstrated the reproducibility of the
341 toxicity assay by targeting another cell type (T-cells) treated with a different apoptotic inducer
342 (staurosporine, Supplementary Fig. 4).

343

344 **2.8. Measurement of tissue dynamics *in vivo*.** To test the application of ADeS in an *in vivo* setting,
345 we applied it to study the response of bystander cells following apoptotic events in the lymph nodes of
346 mice treated with an influenza vaccine. We computed the spatial and temporal coordinates of a
347 neutrophil undergoing apoptosis (Fig. 8A), which, combined with the tracks of neighboring cells, allowed
348 us to characterize cellular response patterns following the apoptotic event. Among other parameters,
349 we observed a sharp decrease in the distance between the neighboring cells and the apoptotic centroid
350 (Fig. 8B) in addition to a pronounced increase in the instantaneous speed of the cells (Fig. 8C).

351

352 Successively, we evaluated the detection of apoptotic cells following laser ablation in the spleen of an
353 anesthetized mouse (Fig. 8D). Previous research has employed this method to study immune cell

354  responses to tissue damage(Uderhardt et al. 2019). The insult caused prompt recruitment of
355  neutrophils, leading to the formation of a local swarm (Fig. 8E, left). After that, the neutrophils within the
356  swarm underwent apoptotic body formation in a coordinated manner (Fig. 8E, right). To quantify this
357  event, we processed the generated time-lapse with ADeS, resulting in a probability map of apoptotic
358  events throughout the acquisition (x,y,t,p; Fig. 8F). Accordingly, the location with the highest probability
359  corresponded to the area damaged by the laser, while the visual representation of the probability map
360  enabled us to infer the morphology and location of the swarm. This result demonstrates the potential
361  application of ADeS in digital pathology, showing how the distribution of apoptotic events throughout
362  the tissue can identify areas enriched by cell death events.

363

364  ## 3. Discussion

365  Automated bio-image analysis obviates the need for manual annotation and avoids bias introduced by
366  the researcher. In this regard, recent studies showed the promising usage of DL to classify static
367  images(Verduijn et al. 2021; Jimenez-Carretero et al. 2018; Kranich et al. 2020) or time-lapses
368  containing single apoptotic cells(Mobiny et al. 2020). However, these approaches are unsuitable for
369  microscopy time-lapses because they do not address two fundamental questions: the location, over the
370  whole field of view, at which an event occurs, and its duration. These questions define a detection
371  task(Zhao et al. 2019) in space and time, which has a computational cost that can rapidly grow with the
372  size and lenght of a movie. Moreover, live-cell imaging data present specific challenges which further
373  increase the difficulty of detection routines, including densely packed fields of view, autofluorescence,
374  and imaging artifacts(Pizzagalli et al. 2018).

375  Consequently, computational tools to effectively detect apoptotic events in live-cell imaging remained
376  unavailable. Thus, we created an apoptosis detection pipeline that could address the abovementioned
377  challenges *in vitro* and *in vivo*. In this regard, ADeS represents a crucial bridge between AR and
378  bioimaging analysis, being the first apoptosis detection routine with demonstrated applicability to full
379  microcopy time-lapses. In addition, we presented two comprehensive and curated datasets
380  encompassing multiple cell types, fluorescent labels, and imaging techniques to encourage
381  reproducibility and foster the development of apoptosis detection routines.

382  In human activity recognition benchmark, 3DCNNs(Vrskova et al. 2022), two-streams networks(Ye et
383  al. 2019), and RNNs(Mohd Noor, Tan, and Ab Wahab 2022) have proved to score the highest accuracy
384  on most kinetic datasets(Ullah et al. 2021). However, in most studies for the classification of apoptosis,
385  authors unanimely employed RNNs such as Conv-LSTMs. This choice, although produced valid results,
386  is not necessarily optimal for the task. In this regard, Ullah and colleagues highlighted that the
387  performances of different DL architectures are highly dependent on the AR dataset(Ullah et al. 2021).
388  Therefore, selecting the most suitable one is only possible after an extensive benchmark. In our
389  comparison, we demonstrated for the first time that attention-based networks are suitable for the
390  classification and detection of apoptotic events. Accordingly, our Conv-Transformer network
391  outperformed DL architectures previously employed in other studies, including 3DCNNs and RNNs.

10

392   This result established a landmark in the application of attention-based networks in AR for live-cell
393   imaging. Moreover, it suggests the possible benefits of employing transformers for the classification of
394   different biological activities other than cell death.

395   Similar to most diagnostic tools, ADeS displayed a tradeoff between sensitivity (TPR) and specificity (1
396   - FPR), which is a known challenge in binary classification(Pang et al. 2021). This tradeoff can be
397   attributed to the fact that apoptosis is rare in normal physiological conditions, leading to a high degree
398   of class imbalance during training. As a result, the choice of the training set had a significant impact on
399   the performances of ADeS. For instance, we highlighted the importance of a training and validation set
400   that included challenges related to real live-cell imaging acquisitions, such as overlapping cells and low
401   signal-to-noise samples. Including these challenges instances enabled ADeS to attain low
402   misclassification rate and robust real-life performanes. Nonetheless, we observed residual
403   misclassifications due to shared similarities between healthy and apoptotic cells. For instance, *in vitro*
404   mitotic divisions could mislead the detection of apoptotic nuclei, while *in vivo*, overlapping cells were
405   sometimes mistaken for apoptotic cells. Therefore, to effectively address these challenges, it is crucial
406   to implement strategies to increase the representativeness of the dataset, such as integrating multiple
407   data sources and data augmentation techniques.

408   From a biological perspective, ADeS has multiple applications in fundamental and clinical research.
409   Among other advantages, it can provide insights into pivotal cell death mechanisms, monitor the
410   therapies used to modulate apoptosis in various diseases and characterize the toxicity of different
411   compounds. In this regard, ADeS readout is analogous to standard fluorescent probes for apoptosis
412   detection, with the advantage that it can be applied directly to nuclear or cytoplasmic staining without
413   the need of additional fluorescent reporters. Therefore, ADeS avoids using any additional acquisition
414   channel, which can be used for multiplexing purposes. Moreover, common probes(Loo 2011; Kyrylkova
415   et al. 2012; Atale et al. 2014; Vermes et al. 1995; Sun et al. 2008) flag early apoptosis stages, activated
416   up to several minutes before the point at which morphological changes in the cell(Green 2005;
417   Takemoto et al. 2003); meanwhile, these cells can reverse the apoptotic process (Masri and
418   Chandrashekhar 2008; Geske et al. 2001; H. L. Tang et al. 2009). By contrast, ADeS indicates the
419   exact instant of cell disruption, thus adding specificity to the spatial-temporal dimension. For these
420   reasons, we suggest that ADeS can complement the information provided by classic apoptotic
421   biomarkers, which will prove advantageous in experimental assays where the temporal resolution
422   delivers more information than the sole apoptotic count. Moreover, ADeS can be usefully applied in
423   processing high-throughput live-cell imaging, minimizing annotation time and research bias.

424   Finally, in tissue dynamics the spatial-temporal activity of cells can reveal connections between
425   signaling pathways and the fate decision of individual cells, such as mitosis or apoptosis(Gagliardi et
426   al. 2021). These intricate systems can display complex dynamics, which can be better comprehended
427   incorporating spatial and temporal coordinates provided by ADeS. Consequently, we propose that
428   integrating these spatial-temporal characteristics with experimental observations could lay the
429   groundwork for understanding the mechanism governing complex signaling pathways. Furthermore, we

430  contend that this information has the potential to facilitate the development of predictive models,
431  establishing a correlation between specific cell death dynamics and the underlying stimuli. This, in turn,
432  could serve as the foundation for innovative diagnostic tools capable of inferring the cause of cell death.

433  In conclusion, ADeS constitutes a novel solution for apoptosis detection that combines state-of-the-art
434  microscopy and DL. Its successful implementation represents a step towards the general application of
435  AR methods to live-cell imaging. By bridging these two distinct fields, ADeS leverages succesfully the
436  benefits of automated routines. Further work could expand the proposed pipeline to encompass diverse
437  cell populations, various types of cell death, and potentially broader cellular activities.

## 4. Material and methods

439  **4.1. MCF10A cell line and image acquisition.** The normal-like mammary epithelial MCF10A cells
440  (provided by Joan Brugge(Debnath, Muthuswamy, and Brugge 2003)), stably expressing the nuclear
441  marker, were generated as previously described(Gagliardi et al. 2021). Briefly, the nuclear marker H2B-
442  miRFP703, provided by Vladislav Verkhusha (Addgene plasmid # 80001)(Shcherbakova et al. 2016),
443  was subcloned in the PiggyBac plasmid pPBbSr2-MCS. After cotransfection with the transposase
444  plasmid(Yusa et al. 2011), cells were selected with 5 µg/ml Blasticidin and subcloned. For time-lapse
445  imaging, the cells were seeded on 5 µg/ml fibronectin (PanReac AppliChem) coated 1.5  glass-bottom
446  24 well plates (Cellvis) at 1 x $10^5$ cells/well density. After 48 hours, when the optical density was
447  reached, the confluent cell monolayer was acquired every 1 or 5 minutes for several hours with a Nikon
448  Eclipse Ti inverted epifluorescence microscope with 640nm LED light source, ET705/72m emission
449  filter and a Plan Apo air 203 (NA 0.8) or a Plan Apo air 403 (NA 0.9) objectives. The collection of
450  biological experiments used in this study includes different stimulation of apoptosis, such as growth
451  factors, serum starvation and doxorubicin at various concentrations.

452  **4.2. Apoptosis induction of MCF10A cells with doxorubicin.** Normal-like mammary epithelial
453  MCF10A cells were grown in 24 well glass coated with fibronectin with a seeding of 1x$10^5$ cells/well.
454  After two days, cells were starved for three hours and treated with doxorubicin at 1.25, 2.50, and 5.00
455  µM concentrations.

456  **4.3. Mice.** Prior to imaging, mice were anesthetized with a cocktail of Ketamine (100 mg/Kg) and
457  Xylazine (10 mg/Kg) as previously described(Sumen et al. 2004). All animals were maintained in
458  specific pathogen-free facilities at the Institute for Research in Biomedicine (Bellinzona, CH). All the
459  experiments were performed according to the regulations of the local authorities and approved by the
460  Swiss Federal Veterinary Office.
461

462  **4.6. Intravital Two-Photon Microscopy.** Surgery in the popliteal lymph node was performed as
463  previously reported(Miller et al. 2004). The exposed organs were imaged on a custom up-right two-
464  photon microscope (TrimScope, LaVision BioTec). Probe excitation and tissue second-harmonic
465  generation (SHG) were achieved with two Ti:sapphire lasers (Chamaleon Ultra I, Chamaleon Ultra II,

466    Coherent) and an optical oscillator that emits in the 1,010–1,340 nm range (Chamaleon Compact OPO,
467    Coherent) and has an output wavelength between 690–1,080 nm.
468

469    **4.5. Neutrophil isolation from mouse bone marrow.** Bone marrow samples were extracted via
470    flushing with PBS from the long bones of UBC-GFP mice (https://www.jax.org/strain/004353). Then, the
471    bone marrow was filtered through a 40um strainer and resuspended in PBS. Primary bone marrow
472    neutrophils were isolated with Ficoll gradient and resuspended in PBS.
473

474    **4.6. T-cell culture in a 3D collagen matrix**. Human CD4+ T cells were isolated from the PBMC fraction
475    of healthy donors obtained from NetCAD (Canadian Blood Services). Cell purity was above 95%. Naïve
476    CD4+ T cells were activated by adding Dynabeads coated with anti-human CD3e/CD28 antibody (1:1
477    bead:cell ratio, Life Technologies Cat #11131D) in RPMI1640 supplemented with 10% FBS (VWR
478    Seradigm Cat #1500-500), 2 mM GlutaMAX (Gibco Cat #3050-061), 1mM sodium pyruvate (Corning
479    Cat #25-000-CI) and 10mM HEPES (Sigma-Aldrich Cat #H4034). After two days, beads were removed
480    and cells were cultured for another 4-6 days in a medium containing 50 IU/mL human rIL-2 (Biotechne
481    Cat #202-IL-500), keeping cell density at $2 \times 10^5$ cells/mL. Cells were used for all experiments between
482    days 6 to 8. All work with human blood has been approved by the University of Manitoba Biomedical
483    Research Ethics Board (BREB).

484    **4.7. Apoptosis live-cell imaging of T-cells in 3D collagen chambers**. T cells were labeled at day 6-
485    8 using CMAC (10µM) cell tracker dye (Invitrogen) and glass slide chambers were constructed as
486    previously described(Lopez et al. 2019; 2022). Briefly, $2 \times 10^6$ cells were mixed in 270µL of bovine
487    collagen (Advanced Biomatrix cat #5005-100ML) at a final concentration of 1.7 mg/mL. Collagen
488    chambers were solidified for 45 minutes at 37°C / 5% CO2 and placed onto a custom-made heating
489    platform attached to a temperature control apparatus (Werner Instruments). For the induction of
490    apoptosis, 1µM of Staurosporine (Sigma Cat #569397-100UG) and 800ng of TNF-a (Biolegend Cat
491    #570104) in 100µL RPMI were added on top of the solidified collagen. Cells were imaged as soon as
492    the addition of apoptosis inducers using a multiphoton microscope with a Ti:sapphire laser (Coherent),
493    tuned to 800 nm for optimized excitation of CMAC. Stacks of 13 optical sections (512 x 512 pixels) with
494    4 mm z-spacing were acquired every 15 seconds to provide imaging volumes of 44mm in depth (with a
495    total time of 60 - 120 minutes). Emitted light was detected through 460 / 50nm, 525 / 70 nm, and 595 /
496    50 nm dichroic filters with non-descanned detectors. All images were acquired using the 20 x 1.0 N.A.
497    Olympus objective lens (XLUMPLFLN; 2.0mm WD).

498    **4.8. Data Processing and Image Analysis.** The raw video data, composed by uint8 or uint16 TIFFs,
499    were stored as HDF5 files. No video pre-processing was applied to the raw data before image analysis.
500    Cell detection, tracking, and volumetric reconstruction of microscopy videos were performed using
501    Imaris (Oxford Instruments, v9.7.2). The resulting data were further analyzed with custom Matlab and
502    Python scripts (see code availability section).
503

**4.9. Apoptosis annotation of epithelial MCf10A cells *in vitro*.** We manually annotated apoptotic events of MCF10A cells by visual inspection of the movies. The annotation was done by observing the morphological changes associated with apoptosis (e.g. nuclear shrinkage, chromatin condensation, epithelial extrusion, nuclear fragmentation) across multiple consecutive frames. Using a custom Fiji(Schindelin et al. 2012) macro, we automatically stored x and y centroids of the apoptotic nucleus. The time t of each apoptotic annotation was defined as the beginning of nuclear shrinkage.

**4.10. Generation of the *in vitro* training dataset**. The 16-bit raw movies were min-max scaled to the 0.001 and 0.999 quantiles and downsampled to 8-bit resolution. Using the database of manually labeled coordinates of apoptotic events (x,y,t), we extracted crops with 59 x 59 pixels resolution (2x scaling for the FOVs acquired with the 20x objective). Seven time-steps of the same location were extracted, with linear spacing from -10 minutes to +50 minutes relative to the apoptosis annotation. This time frame was chosen to capture the cell before the onset of apoptosis, and the morphological changes associated with apoptosis (nuclear shrinkage, decay into apoptotic bodies, extrusion from epithelium). The resulting image cube has dimensions of 59 x 59 x 7. To create the training data for the non-apoptotic class, we excluded areas with an annotated apoptotic event with a safety margin from the movies. From the remaining regions without apoptoses, we extracted image cubes from cells detected with StarDist(Jacquemet et al. 2020) and from random locations. The random crops also included debris, apoptotic bodies from earlier apoptotic events, empty regions, and out-of-focus nuclei.

**4.11. Apoptosis annotation of leukocyte cells *in vivo*.** Three operators independently annotated the videos based on selected morphological criteria. To label apoptotic cells, the annotators considered only the sequences of cells that displayed membrane blebbing followed by apoptotic bodies formation and cell disruption (Fig. 2B). For each frame in the apoptotic sequence, the operators placed a centroid at the center of the cell with the Imaris "Spots" function, generating an apoptotic track. Successively, ground truth tracks were generated according to a majority voting system, and 3D volume reconstruction was performed on ground truth cells using the Imaris "Surface" function. Nearby non-apoptotic cells were also tracked. In addition, other non-apoptotic events were automatically sub-sampled from regions without apoptotic cells.

**4.12. 3D rotation of the *in vivo* annotations.** *In vivo* annotations presented a class unbalance in favor of non-apoptotic cells, with a relative few apoptotic instances. Hence, to compensate for this bias, we produced several representations of the raw data by interpolating the raw image stacks in 3D volumes and rotating them in randomly sampled directions, with rotational degrees between 0° and 45°. After each manipulation, the rotated volume underwent flattening by maximum projection and symmetric padding to preserve the original dimension. The 2D images were successively resized and cropped to match the 59 x 59 pixels input of the classifier. Finally, the training sequences were saved as uint8 gray-scale TIFFs files.

14

**4.13. Generation of the *in vitro* and *in vivo* training datasets**. To detect apoptotic cells in microscopy acquisitions, we defined a 2D binary classification task in which apoptotic events are labeled with class 1, while non-apoptotic events belonged to the class label 0. The resulting unprocessed data consisted of frame sequences composed of 3D crops. The content of the class label 0 in vitro included: healthy nuclei, background, cell debris and mitotic cells. The content of the class label 0 *in vivo* included: motile cells, arrested cells, highly deformed cells, overlapping cells, cell debris or blebs, empty background, noisy background, and collagen.

**4.14. Data augmentation and data loader.** Given the varying length of the training sequences contained in the TIFFs, upon training, we used a custom data loader that uniformly samples the input data and produces sequences with a fixed number of frames. The fixed number of frames was set to 5, corresponding to the frame-length of the shortest apoptotic sequence. During training, each sample underwent horizontal shift, vertical shift, zoom magnification, rotation, and flipping. All data augmentations were performed in python using the Keras library.

**4.15. Deep learning architecture.** As a deep learning classifier, we employed a custom architecture relying on time-distributed convolutional layers stacked on top of a transformer module (Conv-Transformer). The input size consists of 5 single-channel images with 59x59 pixel size. The convolutional network has three layers of size 64, 128, and 256 length. Each layer has a 3x3 kernel, followed by Relu activation, batch normalization, and a dropout set to 0.3. The inclusion of padding preserves the dimension of the input, while 2D max-pooling is at the end of each convolutional block. After 2D max pooling, the output is passed to a transformer module counting 6 attention heads, and successively to a fully connected decision layer. The fully connected network has four layers with 1024, 512,128, and 64 nodes, each one followed by Relu activation and a 0.3 dropout layer. The last layer is a softmax activation, which predicts a decision between the two classes.

**4.16. Training and hyper-parameters.** Our model was trained in TensorFlow with Adam optimizer, using binary cross-entropy loss and an initial learning rate of 0.0001. The optimal mini-batch size was 32, and the number of training epochs was 200. In training mode, we set a checkpoint to save the model with the best accuracy on the validation dataset, and a checkpoint for early stopping with patience set to 15 epochs. In addition, the learning rate decreased when attending a plateau.

**4.17. ADeS deployment** For the deployment of the classifier on microscopy videos, we generative region proposals using the selective search algorithm, obtaining a set of ROIs for each candidate frame of the input movie. For each ROI computed by the region proposal at time t, a temporal sequence is cropped around t and classified with the Conv-Transformer. The resulting bounding boxes are filtered according to a probability threshold and processed with the non-maxima suppression utils from Pytorch. Consecutive bounding boxes classified as apoptotic are connected using a custom multi-object tracking algorithm based on Euclidean distance. The generated trajectories are filtered by discarding those with less than two objects.

15

583

584 **4.18. Default and user-defined parameters.** ROIs detected with the region proposal are filtered

585 according to their size, discarding the ones with edges below 20 pixels and above 40 pixels.

586 Furthermore, a threshold on intensity is applied to exclude uint8 patches with an average brightness

587 below 40. Upon classification, a temporal window corresponding to the expected duration of the

588 apoptotic event is set by the user (9 frames by default). This temporal window is subsampled to match

589 the number of input frame of the classifier (5). The filtering of the predictions depends on a user-

590 specified threshold, which by default corresponds to 0.95 *in vivo* and 0.995 *in vitro*. Non-maxima

591 suppression is based on the overlapping area between bounding boxes, set to 0.1 by default. The

592 centroid tracking has the following adjustable parameters: gap and distance threshold. The "gap"

593 parameter, set to three frames, specifies for how long a centroid can disappear without being attributed

594 a new ID upon reappearance. A threshold on the distance, set by default to 10 pixels, allows the

595 connection of centroids within the specified radius. All the reported quantifications had default

596 parameters.

597 **4.19. Statistical analyses.** Statistical comparisons and plotting were performed using GraphPad Prism

598 8 (Graphpad, La Jolla, USA). All statistical tests were performed using non-parametric Kruskal-Wallis

599 test or Mann-Witney test For significance, p value is represented as * when $p < 0.05$, ** when $p < 0.005$

600 and *** when $p < 0.0005$.

## 601 5. Aknowledgements

616

617 **5.2. Authors contributions**

618 Conceptualization: SG, DU, AP

619 Methodology: AP, DU

620 Experiments: PG, PA, MP, RZ, PL

621 Data annotation: PG, AP, LH, DU, PC

16

622    Data analysis and visualization: AP, LH, AG

623    Figures: AP, PG, LH

624    Testing and validation: AP, LH, AG

625    Supervision: SG, DU,  RK, LG, OP, TM, MT

626    Writing—original draft: AP, PC, DU, PG

627    Writing—review & editing: AP, SG

628

629    **5.3. Competing interests**

630    Authors declare that they have no competing interest.

631

632

633

634    **6. Bibliography**

635

636    Adadi, Amina. 2021. "A Survey on Data-efficient Algorithms in Big Data Era." *Journal of Big Data* 8 (1).

637        https://doi.org/10.1186/s40537-021-00419-9.

638    Atale, N., S. Gupta, U. C.S. Yadav, and V. Rani. 2014. "Cell-Death Assessment by Fluorescent and

639        Nonfluorescent Cytosolic and Nuclear Staining Techniques." *Journal of Microscopy* 255 (1): 7–19.

640        https://doi.org/10.1111/jmi.12133.

641    Beltman, Joost B, Athanasius F M Marée, Rob J de Boer, Athanasius F M Marée, Rob J de Boer, Athanasius F

642        M Marée, and Rob J de Boer. 2009. "Analysing Immune Cell Migration." *Nature Reviews. Immunology* 9

643        (11): 789–98. https://doi.org/10.1038/nri2638.

644    Coleman, Mathew L., Erik A. Sahai, Margaret Yeo, Marta Bosch, Ann Dewar, and Michael F. Olson. 2001.

645        "Membrane Blebbing during Apoptosis Results from Caspase-Mediated Activation of ROCK I." *Nature Cell*

646        *Biology* 3 (4). https://doi.org/10.1038/35070009.

647    D'Arcy, Mark S. 2019. "Cell Death: A Review of the Major Forms of Apoptosis, Necrosis and Autophagy." *Cell*

648        *Biology International*. https://doi.org/10.1002/cbin.11137.

649    Damián La Greca, Alejandro, Nelba Pérez, Sheila Castañeda, Paula Melania Milone, María Agustina Scarafía,

650        Alan Miqueas Möbbs, Ariel Waisman, et al. 2021. "Celldeath: A Tool for Detection of Cell Death in

651        Transmitted Light Microscopy Images by Deep Learning-Based Visual Recognition." *PLoS ONE* 16 (6

652        June). https://doi.org/10.1371/journal.pone.0253666.

653    Darzynkiewicz, Zbigniew, Dariusz Galkowski, and Hong Zhao. 2008. "Analysis of Apoptosis by Cytometry Using

654        TUNEL Assay." *Methods* 44 (3). https://doi.org/10.1016/j.ymeth.2007.11.008.

655    Debnath, Jayanta, Senthil K. Muthuswamy, and Joan S. Brugge. 2003. "Morphogenesis and Oncogenesis of

656        MCF-10A Mammary Epithelial Acini Grown in Three-Dimensional Basement Membrane Cultures."

657        *Methods*. https://doi.org/10.1016/S1046-2023(03)00032-X.

658    Elmore, Susan. 2007. "Apoptosis: A Review of Programmed Cell Death." *Toxicologic Pathology*.

659        https://doi.org/10.1080/01926230701320337.

660    Eom, Young Woo, Mi Ae Kim, Seok Soon Park, Mi Jin Goo, Hyuk Jae Kwon, Seonghyang Sohn, Wook Hwan

661        Kim, Gyesoon Yoon, and Kyeong Sook Choi. 2005. "Two Distinct Modes of Cell Death Induced by

662        Doxorubicin: Apoptosis and Cell Death through Mitotic Catastrophe Accompanied by Senescence-like

663        Phenotype." *Oncogene* 24 (30). https://doi.org/10.1038/sj.onc.1208627.

664    Fesik, Stephen W. 2005. "Promoting Apoptosis as a Strategy for Cancer Drug Discovery." *Nature Reviews*

665         *Cancer*. https://doi.org/10.1038/nrc1736.

666   Flier, Laurens G. Van Der, and Hans Clevers. 2009. "Stem Cells, Self-Renewal, and Differentiation in the
667         Intestinal Epithelium." *Annual Review of Physiology*.
668         https://doi.org/10.1146/annurev.physiol.010908.163145.

669   Fox, Sarah, Andrew E. Leitch, Rodger Duffin, Christopher Haslett, and Adriano G. Rossi. 2010. "Neutrophil
670         Apoptosis: Relevance to the Innate Immune Response and Inflammatory Disease." *Journal of Innate*
671         *Immunity*. https://doi.org/10.1159/000284367.

672   Gagliardi, Paolo Armando, Maciej Dobrzyński, Marc Antoine Jacques, Coralie Dessauges, Pascal Ender,
673         Yannick Blum, Robert M. Hughes, Andrew R. Cohen, and Olivier Pertz. 2021. "Collective ERK/Akt Activity
674         Waves Orchestrate Epithelial Homeostasis by Driving Apoptosis-Induced Survival." *Developmental Cell* 56
675         (12). https://doi.org/10.1016/j.devcel.2021.05.007.

676   Galluzzi, Lorenzo, Ilio Vitale, Stuart A. Aaronson, John M. Abrams, Dieter Adam, Patrizia Agostinis, Emad S.
677         Alnemri, et al. 2018. "Molecular Mechanisms of Cell Death: Recommendations of the Nomenclature
678         Committee on Cell Death 2018." *Cell Death and Differentiation*. https://doi.org/10.1038/s41418-017-0012-4.

679   Geske, F. J., R. Lieberman, R. Strange, and L. E. Gerschenson. 2001. "Early Stages of P53-Induced Apoptosis
680         Are Reversible." *Cell Death and Differentiation* 8 (2). https://doi.org/10.1038/sj.cdd.4400786.

681   Girshick, Ross. 2015. "Fast R-CNN." In *Proceedings of the IEEE International Conference on Computer Vision*.
682         https://doi.org/10.1109/ICCV.2015.169.

683   Green, Douglas R. 2005. "Apoptotic Pathways: Ten Minutes to Dead." *Cell*.
684         https://doi.org/10.1016/j.cell.2005.05.019.

685   Helmchen, Fritjof, and Winfried Denk. 2005. "Deep Tissue Two-Photon Microscopy." *Nature Methods*.
686         https://doi.org/10.1038/nmeth818.

687   Hotchkiss, Richard S., and Donald W. Nicholson. 2006. "Apoptosis and Caspases Regulate Death and
688         Inflammation in Sepsis." *Nature Reviews Immunology*. https://doi.org/10.1038/nri1943.

689   Jacquemet, Guillaume, Elnaz Fazeli, Nathan H. Roy, Gautier Follain, Romain F. Laine, Lucas von Chamier,
690         Pekka E. Hänninen, John E. Eriksson, and Jean Yves Tinevez. 2020. "Automated Cell Tracking Using
691         StarDist and TrackMate." *F1000Research* 9. https://doi.org/10.12688/f1000research.27019.1.

692   Jensen, Ellen C. 2012. "Use of Fluorescent Probes: Their Effect on Cell Biology and Limitations." *Anatomical*
693         *Record*. https://doi.org/10.1002/ar.22602.

694   Jimenez-Carretero, Daniel, Vahid Abrishami, Laura Fernández-de-Manuel, Irene Palacios, Antonio Quílez-
695         Álvarez, Alberto Díez-Sánchez, Miguel A. del Pozo, and María C. Montoya. 2018. "Tox_(R)CNN: Deep
696         Learning-Based Nuclei Profiling Tool for Drug Toxicity Screening." *PLoS Computational Biology* 14 (11).
697         https://doi.org/10.1371/journal.pcbi.1006238.

698   Jin, Jenny, Kenji Schorpp, Daniel Samaga, Kristian Unger, Kamyar Hadian, and Brent R. Stockwell. 2022.
699         "Machine Learning Classifies Ferroptosis and Apoptosis Cell Death Modalities with TfR1 Immunostaining."
700         *ACS Chemical Biology* 17 (3). https://doi.org/10.1021/acschembio.1c00953.

701   Kabir, Md Alamgir, Ashish Kharel, Saloni Malla, Zachary Joseph Kreis, Peuli Nath, Jared Neil Wolfe, Marwa
702         Hassan, et al. 2022. "Automated Detection of Apoptotic versus Nonapoptotic Cell Death Using Label-Free
703         Computational Microscopy." *Journal of Biophotonics* 15 (4). https://doi.org/10.1002/jbio.202100310.

704   Kranich, Jan, Nikolaos Kosmas Chlis, Lisa Rausch, Ashretha Latha, Martina Schifferer, Tilman Kurz, Agnieszka
705         Foltyn-Arfa Kia, Mikael Simons, Fabian J. Theis, and Thomas Brocker. 2020. "In Vivo Identification of
706         Apoptotic and Extracellular Vesicle-Bound Live Cells Using Image-Based Deep Learning." *Journal of*
707         *Extracellular Vesicles* 9 (1). https://doi.org/10.1080/20013078.2020.1792683.

708   Kyrylkova, Kateryna, Sergiy Kyryachenko, Mark Leid, and Chrissa Kioussi. 2012. "Detection of Apoptosis by
709         TUNEL Assay." *Methods in Molecular Biology* 887. https://doi.org/10.1007/978-1-61779-860-3_5.

710  Loo, Deryk T. 2011. "In Situ Detection of Apoptosis by the TUNEL Assay: An Overview of Techniques." *Methods*
711      *in Molecular Biology* 682. https://doi.org/10.1007/978-1-60327-409-8_1.
712  Lopez, Paul, Oluwaseun Ajibola, Amelie Pagliuzza, Romaniya Zayats, Wan Hon Koh, Alon Herschhorn, Nicolas
713      Chomont, and Thomas T. Murooka. 2022. "T Cell Migration Potentiates HIV Infection by Enhancing Viral
714      Fusion and Integration." *Cell Reports* 38 (8). https://doi.org/10.1016/j.celrep.2022.110406.
715  Lopez, Paul, Wan Hon Koh, Ryan Hnatiuk, and Thomas T. Murooka. 2019. "HIV Infection Stabilizes
716      Macrophage-T Cell Interactions To Promote Cell-Cell HIV Spread." *Journal of Virology* 93 (18).
717      https://doi.org/10.1128/jvi.00805-19.
718  Masri, Carolina, and Y. Chandrashekhar. 2008. "Apoptosis: A Potentially Reversible, Meta-Stable State of the
719      Heart." *Heart Failure Reviews*. https://doi.org/10.1007/s10741-007-9069-3.
720  Miller, Mark J., Arsalan S. Hejazi, Sindy H. Wei, Michael D. Cahalan, and Ian Parker. 2004. "T Cell Repertoire
721      Scanning Is Promoted by Dynamic Dendritic Cell Behavior and Random T Cell Motility in the Lymph Node."
722      *Proceedings of the National Academy of Sciences of the United States of America* 101 (4).
723      https://doi.org/10.1073/pnas.0306407101.
724  Mobiny, Aryan, Hengyang Lu, Hien V. Nguyen, Badrinath Roysam, and Navin Varadarajan. 2020. "Automated
725      Classification of Apoptosis in Phase Contrast Microscopy Using Capsule Network." *IEEE Transactions on*
726      *Medical Imaging* 39 (1): 1–10. https://doi.org/10.1109/TMI.2019.2918181.
727  Mohd Noor, Mohd Halim, Sen Yan Tan, and Mohd Nadhir Ab Wahab. 2022. "Deep Temporal Conv-LSTM for
728      Activity Recognition." *Neural Processing Letters* 54 (5). https://doi.org/10.1007/s11063-022-10799-5.
729  Opferman, J. T. 2008. "Apoptosis in the Development of the Immune System." *Cell Death and Differentiation*.
730      https://doi.org/10.1038/sj.cdd.4402182.
731  Pang, Guansong, Chunhua Shen, Longbing Cao, and Anton Van Den Hengel. 2021. "Deep Learning for Anomaly
732      Detection: A Review." *ACM Computing Surveys*. https://doi.org/10.1145/3439950.
733  Pizzagalli, Diego Ulisse, Yagmur Farsakoglu, Miguel Palomino-Segura, Elisa Palladino, Jordi Sintes, Francesco
734      Marangoni, Thorsten R. Mempel, et al. 2018. "Data Descriptor: Leukocyte Tracking Database, a Collection
735      of Immune Cell Tracks from Intravital 2-Photon Microscopy Videos." *Scientific Data* 5: 1–13.
736      https://doi.org/10.1038/sdata.2018.129.
737  Pizzagalli, Diego Ulisse, Alain Pulfer, Marcus Thelen, Rolf Krause, and Santiago Fernandez Gonzalez. n.d. "A
738      Review on Activities of Immune Cells Observed via Intravital Microscopy." *In Preparation*.
739  Poppe, Ronald. 2010. "A Survey on Vision-Based Human Action Recognition." *Image and Vision Computing* 28
740      (6): 976–90. https://doi.org/10.1016/j.imavis.2009.11.014.
741  Rocheleau, Jonathan V., and David W. Piston. 2003. "Two-Photon Excitation Microscopy for the Study of Living
742      Cells and Tissues." *Current Protocols in Cell Biology* 20 (1).
743      https://doi.org/10.1002/0471143030.cb0411s20.
744  Saraste, Antti, and Kari Pulkki. 2000. "Morphologic and Biochemical Hallmarks of Apoptosis." *Cardiovascular*
745      *Research*. https://doi.org/10.1016/S0008-6363(99)00384-3.
746  Schindelin, Johannes, Ignacio Arganda-Carreras, Erwin Frise, Verena Kaynig, Mark Longair, Tobias Pietzsch,
747      Stephan Preibisch, et al. 2012. "Fiji: An Open-Source Platform for Biological-Image Analysis." *Nature*
748      *Methods*. https://doi.org/10.1038/nmeth.2019.
749  Schmid, Ingrid, Christel Uittenbogaart, and Beth D. Jamieson. 2007. "Live-Cell Assay for Detection of Apoptosis
750      by Dual-Laser Flow Cytometry Using Hoechst 33342 and 7-Amino-Actinomycin D." *Nature Protocols* 2 (1):
751      187–90. https://doi.org/10.1038/nprot.2006.458.
752  Schnell, Ulrike, Freark Dijk, Klaas A. Sjollema, and Ben N.G. Giepmans. 2012. "Immunolabeling Artifacts and the
753      Need for Live-Cell Imaging." *Nature Methods*. https://doi.org/10.1038/nmeth.1855.
754  Secklehner, Judith, Cristina Lo Celso, and Leo M. Carlin. 2017. "Intravital Microscopy in Historic and

755     Contemporary Immunology." *Immunology and Cell Biology*. https://doi.org/10.1038/icb.2017.25.

756   Shalini, S., L. Dorstyn, S. Dawar, and S. Kumar. 2015. "Old, New and Emerging Functions of Caspases." *Cell*

757     *Death and Differentiation*. https://doi.org/10.1038/cdd.2014.216.

758   Shcherbakova, Daria M., Mikhail Baloban, Alexander V. Emelyanov, Michael Brenowitz, Peng Guo, and Vladislav

759     V. Verkhusha. 2016. "Bright Monomeric Near-Infrared Fluorescent Proteins as Tags and Biosensors for

760     Multiscale Imaging." *Nature Communications* 7. https://doi.org/10.1038/ncomms12405.

761   Shi, Xingjian, Zhourong Chen, Hao Wang, Dit Yan Yeung, Wai Kin Wong, and Wang Chun Woo. 2015.

762     "Convolutional LSTM Network: A Machine Learning Approach for Precipitation Nowcasting." In *Advances in*

763     *Neural Information Processing Systems*, 2015-Janua:802–10.

764   Sumen, Cenk, Thorsten R. Mempel, Irina B. Mazo, and Ulrich H. Von Andrian. 2004. "Intravital Microscopy:

765     Visualizing Immunity in Context." *Immunity*. https://doi.org/10.1016/j.immuni.2004.08.006.

766   Sun, Lei, Tongsheng Chen, Longxiang Wang, and Huiying Wang. 2008. "Analysis of Caspase3 Activation in

767     ChanSu-Induced Apoptosis of ASTC-a-1 Cells by Fluorescence Techniques." In *Biophotonics and Immune*

768     *Responses III*. Vol. 6857. https://doi.org/10.1117/12.761422.

769   Takemoto, Kiwamu, Takeharu Nagai, Atsushi Miyawaki, and Masayuki Miura. 2003. "Spatio-Temporal Activation

770     of Caspase Revealed by Indicator That Is Insensitive to Environmental Effects." *Journal of Cell Biology* 160

771     (2). https://doi.org/10.1083/jcb.200207111.

772   Tang, Daolin, Rui Kang, Tom Vanden Berghe, Peter Vandenabeele, and Guido Kroemer. 2019. "The Molecular

773     Machinery of Regulated Cell Death." *Cell Research*. https://doi.org/10.1038/s41422-019-0164-5.

774   Tang, H. L., K. L. Yuen, H. M. Tang, and M. C. Fung. 2009. "Reversibility of Apoptosis in Cancer Cells." *British*

775     *Journal of Cancer* 100 (1). https://doi.org/10.1038/sj.bjc.6604802.

776   Uderhardt, Stefan, Andrew J. Martins, John S. Tsang, Tim Lämmermann, and Ronald N. Germain. 2019.

777     "Resident Macrophages Cloak Tissue Microlesions to Prevent Neutrophil-Driven Inflammatory Damage."

778     *Cell* 177 (3). https://doi.org/10.1016/j.cell.2019.02.028.

779   Uijlings, J. R.R., K. E.A. Van De Sande, T. Gevers, and A. W.M. Smeulders. 2013. "Selective Search for Object

780     Recognition." *International Journal of Computer Vision* 104 (2): 154–71. https://doi.org/10.1007/s11263-

781     013-0620-5.

782   Ullah, Hadiqa Aman, Sukumar Letchmunan, M. Sultan Zia, Umair Muneer Butt, and Fadratul Hafinaz Hassan.

783     2021. "Analysis of Deep Neural Networks for Human Activity Recognition in Videos - A Systematic

784     Literature Review." *IEEE Access*. https://doi.org/10.1109/ACCESS.2021.3110610.

785   Verduijn, Joost, Louis Van der Meeren, Dmitri V. Krysko, and André G. Skirtach. 2021. "Deep Learning with

786     Digital Holographic Microscopy Discriminates Apoptosis and Necroptosis." *Cell Death Discovery* 7 (1).

787     https://doi.org/10.1038/s41420-021-00616-8.

788   Vermes, István, Clemens Haanen, Helga Steffens-Nakken, and Chris Reutellingsperger. 1995. "A Novel Assay

789     for Apoptosis Flow Cytometric Detection of Phosphatidylserine Expression on Early Apoptotic Cells Using

790     Fluorescein Labelled Annexin V." *Journal of Immunological Methods* 184 (1). https://doi.org/10.1016/0022-

791     1759(95)00072-I.

792   Vicar, Tomas, Martina Raudenska, Jaromir Gumulec, and Jan Balvan. 2020. "The Quantitative-Phase Dynamics

793     of Apoptosis and Lytic Cell Death." *Scientific Reports* 10 (1). https://doi.org/10.1038/s41598-020-58474-w.

794   Vrskova, Roberta, Robert Hudec, Patrik Kamencay, and Peter Sykora. 2022. "Human Activity Classification

795     Using the 3DCNN Architecture." *Applied Sciences (Switzerland)* 12 (2).

796     https://doi.org/10.3390/app12020931.

797   Xu, Ju, Mengzhang Li, and Zhanxing Zhu. 2020. "Automatic Data Augmentation for 3d Medical Image

798     Segmentation." In *Lecture Notes in Computer Science (Including Subseries Lecture Notes in Artificial*

799     *Intelligence and Lecture Notes in Bioinformatics)*, 12261 LNCS:378–87. https://doi.org/10.1007/978-3-030-

800      59710-8_37.

801    Ye, W., J. Cheng, F. Yang, and Y. Xu. 2019. "Two-Stream Convolutional Network for Improving Activity

802        Recognition Using Convolutional Long Short-Term Memory Networks." *IEEE Access* 7.

803        https://doi.org/10.1109/ACCESS.2019.2918808.

804    Yusa, Kosuke, Liqin Zhou, Meng Amy Li, Allan Bradley, and Nancy L. Craig. 2011. "A Hyperactive PiggyBac

805        Transposase for Mammalian Applications." *Proceedings of the National Academy of Sciences of the United*

806        *States of America* 108 (4). https://doi.org/10.1073/pnas.1008322108.

807    Zhao, Zhong Qiu, Peng Zheng, Shou Tao Xu, and Xindong Wu. 2019. "Object Detection with Deep Learning: A

808        Review." *IEEE Transactions on Neural Networks and Learning Systems*.

809        https://doi.org/10.1109/TNNLS.2018.2876865.

810    Zhuang, Xinrui, Yuexiang Li, Yifan Hu, Kai Ma, Yujiu Yang, and Yefeng Zheng. 2019. "Self-Supervised Feature

811        Learning for 3d Medical Images by Playing a Rubik's Cube." In *Lecture Notes in Computer Science*

812        *(Including Subseries Lecture Notes in Artificial Intelligence and Lecture Notes in Bioinformatics)*, 11767

813        LNCS:420–28. https://doi.org/10.1007/978-3-030-32251-9_46.

814

## 815  7. Tables

816

817    **Table 1. Comparison of deep learning architectures for apoptosis classification.** *Comparative table reporting*

818    *accuracy, F1 and AUC metrics for a CNN, 3DCNN, Conv-LSTM, and Conv-Transformer. The classification*

819    *accuracy is reported for static frames or image-sequences. N.A. stands for non applicable. The last column shows*

820    *which cell death study employed the same baseline architecture displayed in the table..*

| Classifier architecture | Frame accuracy | Sequence accuracy | F1 | AUC | Study |
|---|---|---|---|---|---|
| CNN | 74 % ± 1.3 | N.A. | 0.77 | 0.779 | (Damián La Greca et al. 2021; Verduijn et al. 2021) |
| 3DCNN | N.A. | 91.22 %± 0.15 | 0.91 | 0.924 | - |
| Conv-LSTM | N.A. | 97.42 % ± 0.09 | 0.97 | 0.994 | (Mobiny et al. 2020; Kabir et al. 2022) |
| Conv-Transformer | N.A | 98.27 % ± 0.25 | 0.98 | 0.997 | Our |

821

822

823    **Table 2. Comparison of cell death identification studies.** *Table reporting all studies on cell death classification*
824    *based on machine learning. For each study, we included the reported classification accuracy, the experimental*
825    *conditions of the studies, the target input of the classifier, and the capability of performing detection on static frames*
826    *or microscopy time-lapses. Met conditions are indicated with a green check. Moreover, for each study we reported*
827    *the architecture of the classifier and the number of apoptotic cells in the training set. N.A. stands for not available*
828    *and indicates that the information is not reported in the study.*

| Study | Input of the classifier | Reported classification accuracy | *In vitro* | *In vivo* | Detection In frame | Detection in movies | Classifier architecture | N cell death |
|---|---|---|---|---|---|---|---|---|
| Our | Frame sequence | 98.27 % | ✓ | ✓ | ✓ | ✓ | Conv-Transformer | 13'120 |
| (Jin et al. 2022) | Frame | 93 % | ✓ | ✗ | ✗ | ✗ | Logistic regression | N.A. |
| (Verduijn et al. 2021) | Frame | 87 % | ✓ | ✗ | ✗ | ✗ | VGG-19 | 19'339 |

| | | | | | | | | |
|---|---|---|---|---|---|---|---|---|
| (Kabir et al. 2022) | Frame sequence | 93 % | ✓ | ✗ | ✗ | ✗ | ResNet101-LSTM | 3'172 |
| (Damián La Greca et al. 2021) | Frame | 96.58 % | ✓ | ✗ | ✗ | ✗ | ResNet50 | 11'036 |
| (Mobiny et al. 2020) | Frame sequence | 93.8 % | ✓ | ✗ | ✗ | ✗ | CapsNet-LSTM | 41'000 |
| (Kranich et al. 2020) | Frame | 93.2 % | ✓ | ✗ | ✗ | ✗ | CAE-RandomForest | 27'224 |
| (Vicar et al. 2020) | Frame sequence | N.A. | ✓ | ✗ | ✓ | ✓ | biLSTM | 1'745 |
| (Jimenez-Carretero et al. 2018) | Frame | N.A. | ✓ | ✗ | ✓ | ✗ | R-CNN | 255'215 |

829

830 **8. Figures**

22
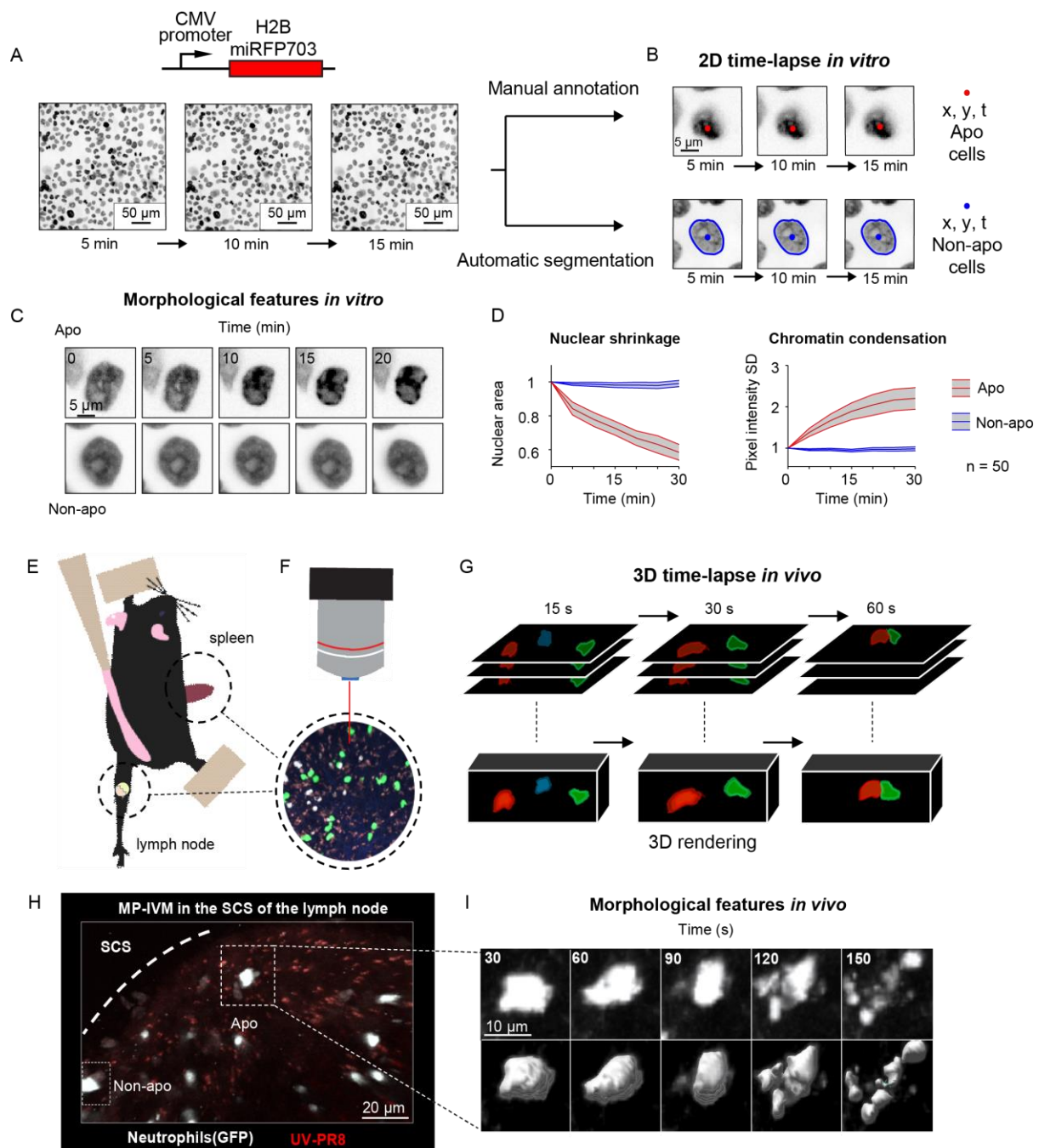
**Figure 1: Generation of in vitro and in vivo live-cell imaging data. A.** *Microphotographs depicting mammary epithelial MCF10A cells transduced with H2B-miRFP703 marker and grown to form a confluent monolayer. The monolayer was acquired with a fluorescence microscope for several hours with 1-, 2- or 5-min time resolution. **B.** The centroid (x, y) and the time (t) of apoptotic events were annotated manually based on morphological features associated with apoptosis. Non-apoptotic cells were identified by automatic segmentation of nuclei. **C.** Image time-lapses showing a prototypical apoptotic event (**upper panels**), with nuclear shrinkage and chromatin condensation, and a non-apoptotic event (**bottom panels**). **D.** Charts showing the quantification of nuclear size (**left**) and the standard deviation of the nuclear pixel intensity (right) of apoptotic and non-apoptotic cells (n = 50). Central darker lines represent the mean, gray shades bordered by light colored lines represent the standard deviation. **E.** Simplified drawing showing the surgical set-up for lymph node and spleen. **F-G.** Organs are subsequently imaged*

23

843 *with intravital 2-photon microscopy (IV-2PM, **F**), generating 3D time-lapses (**G**). **H.** Representative IV-2PM*
844 *micrograph and **I.** selected crops showing GFP-expressing neutrophils (white) undergoing apoptosis. The*
845 *apoptosis sequence is depicted by raw intensity signal (**upper panels**) and 3D surface reconstruction (**bottom***
846 ***panels**).*

847



848
849
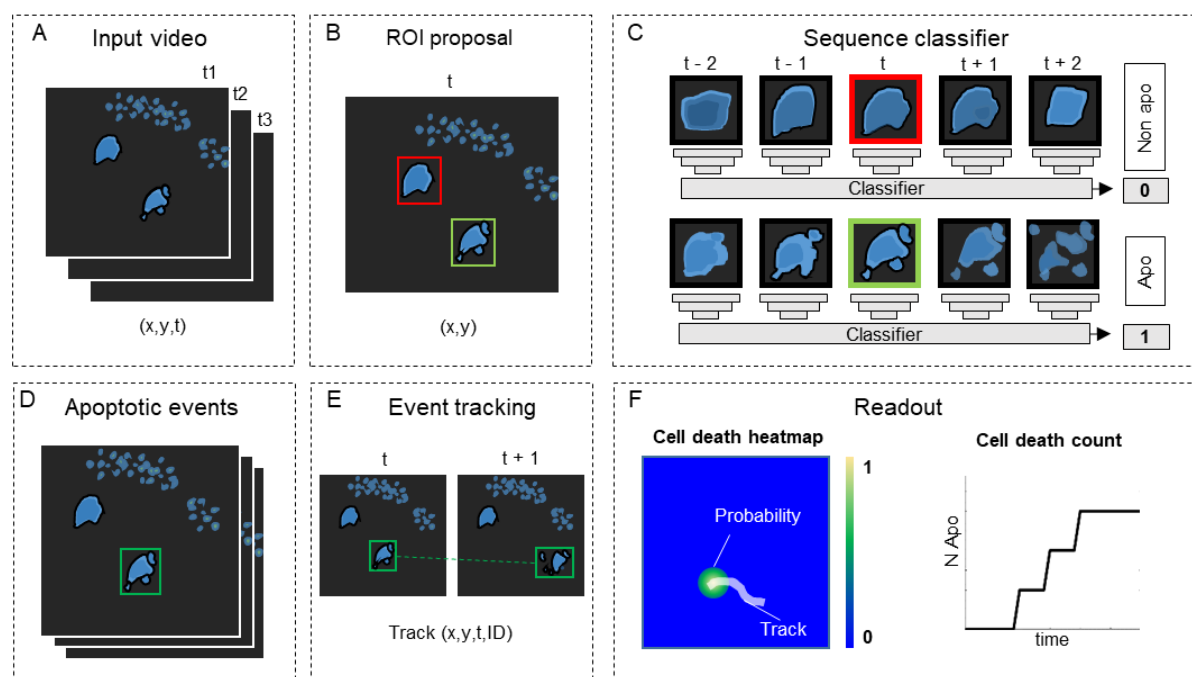
850 **Figure 2. ADeS, a pipeline for apoptosis detection. A.** *ADeS input consists of single channel 2D microscopy*
851 *videos (x,y,t) **B.** Each video frame is pre-processed to compute the candidate Regions of Interest (ROI) with a*
852 *selective search algorithm. **C.** Given the coordinates of the ROI at time t, ADeS extracts a series of snapshots*
853 *ranging from t-n to t+n. A deep learning network classifies the sequence either as non-apoptotic (0) or apoptotic*
854 *(1). **D.** The predicted apoptotic events are labelled at each frame by a set of bounding boxes which, **E.** are*
855 *successively linked in time with a tracking algorithm based on euclidean distance. **F.** The readout of ADeS consist*
856 *of bounding boxes and associated probabilities, which can generate a probability map of apoptotic events over the*
857 *course of the video (**left**) as well as providing the number of apoptotic events over time (**right**).*

858
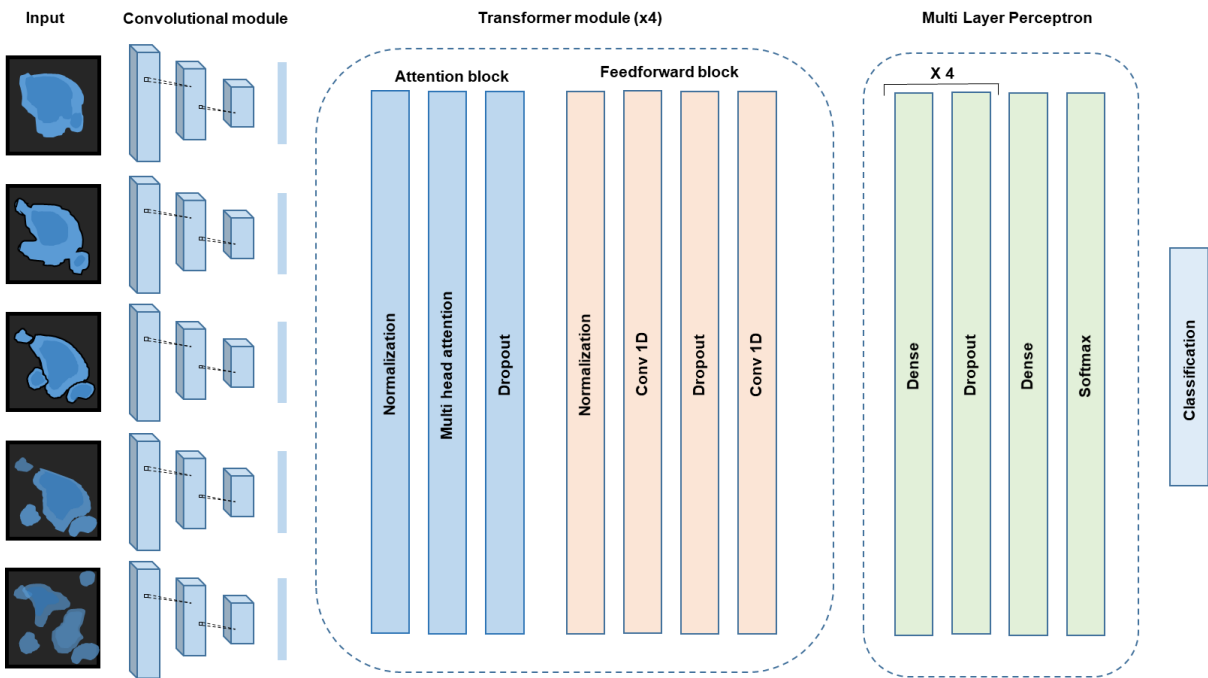
859
860 ***Figure 3. Conv-Transformer architecture at the chore of ADeS.*** *Abstracted representation of the proposed*
861 *Conv-Transformer classifier. The input sequence of frames is processed with warped convolutional layers, which*
862 *extract the features of the images. The extracted features are passed into the 4 transformer modules, composed*
863 *of attention and feedforward blocks. Finally, a multi layer perceptron enables classification between apoptotic and*
864 *non-apoptotic sequences.*
865
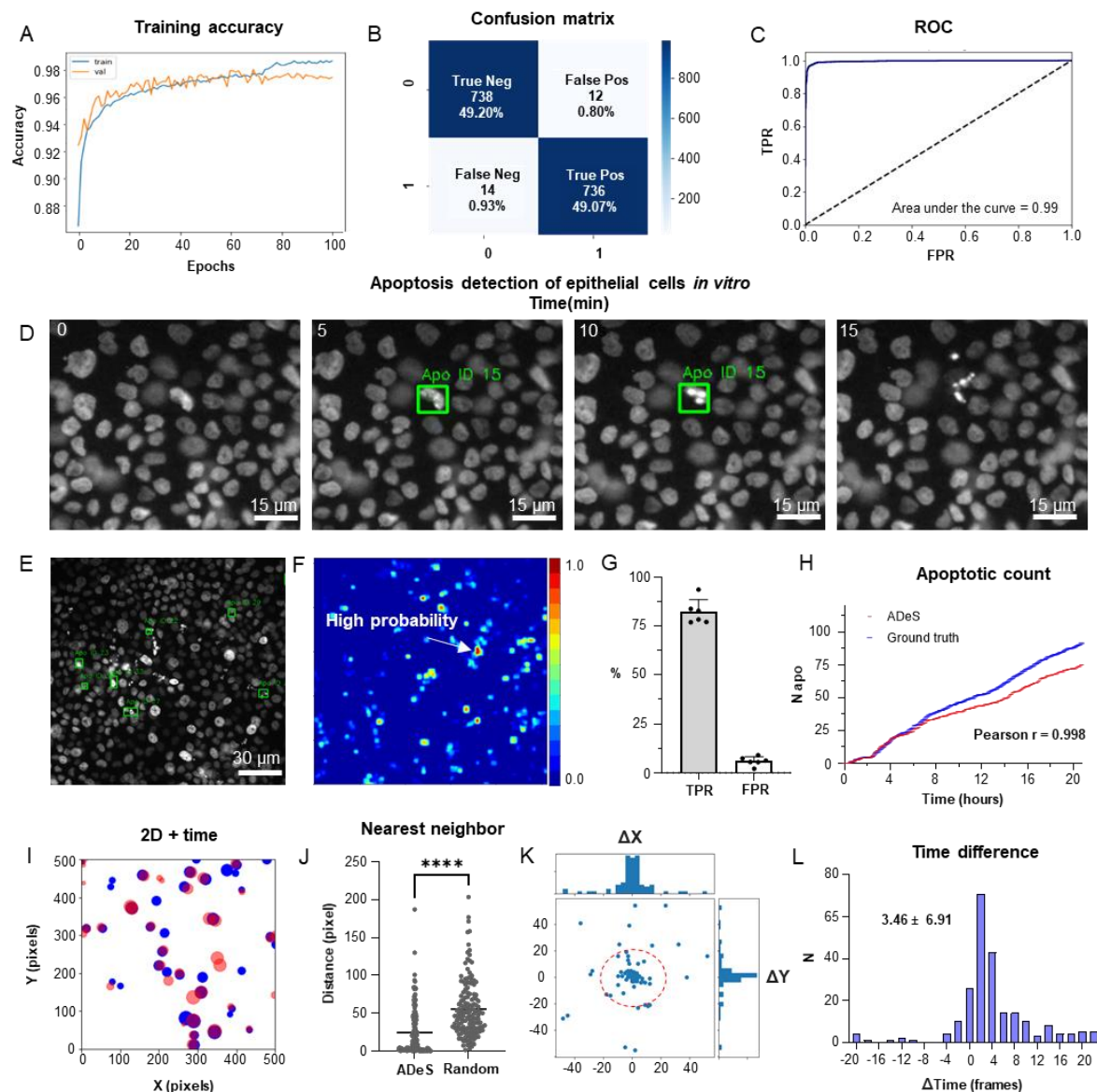
**Figure 4. Training and performance in vitro. A.** Confusion matrix of the trained model at a decision-making threshold of 0.5. **B.** Receiver operating characteristic displaying the false positive rate (specificity) corresponding to each true positive rate (sensitivity). **C.** Training accuracy of the final model after 100 epochs of training. **D.** Representative example of apoptosis detection in a time-lapse acquired in vitro. **E.** Multiple detection of nuclei undergoing apoptosis displays high sensitivity in densely packed field of views. **F.** Heatmap representation depicting all apoptotic events in a movie and the respective probabilities. **G.** Bar plots showing the true positive rate (TPR) and false positive rate (FPR) of ADeS applied to five testing movies, each one depicting an average of 98 apoptosis. **H.** Time course showing the cumulative sum of ground truth apoptosis (blue) and correct predictions (red). **I.** 2D visualization of spatial-temporal coordinates of ground truth (blue) and predicted apoptosis (red). In the 2D representation, the radius of the circles maps the temporal coordinates of the event. **J.** Pixel distance between ADeS predictions and the nearest neighbor (NN) of the ground truth (left) in comparison with the NN distance obtained from a random distribution (right). The plot depicts all predictions of ADeS, including true positives and false positives. **K.** Scatterplot of the spatial distance between ground truth and true positives of ADeS. Ground truth points are centered on the X = 0 and Y = 0 coordinates. **L. Distribution of** the temporal distance (frames) of the

26

882 *correct predictions from the respective ground truth nearest neighbor. Statistical comparison was performed with*

883 *Mann-Whitney test. Columns and error bars represent the mean and standard deviation respectively. Statistical*

884 *significance is expressed as: p ≤ 0.05 (\*), p ≤ 0.01 (\*\*), p ≤ 0.001 (\*\*\*), p ≤ 0.0001 (\*\*\*\*).*

885



886
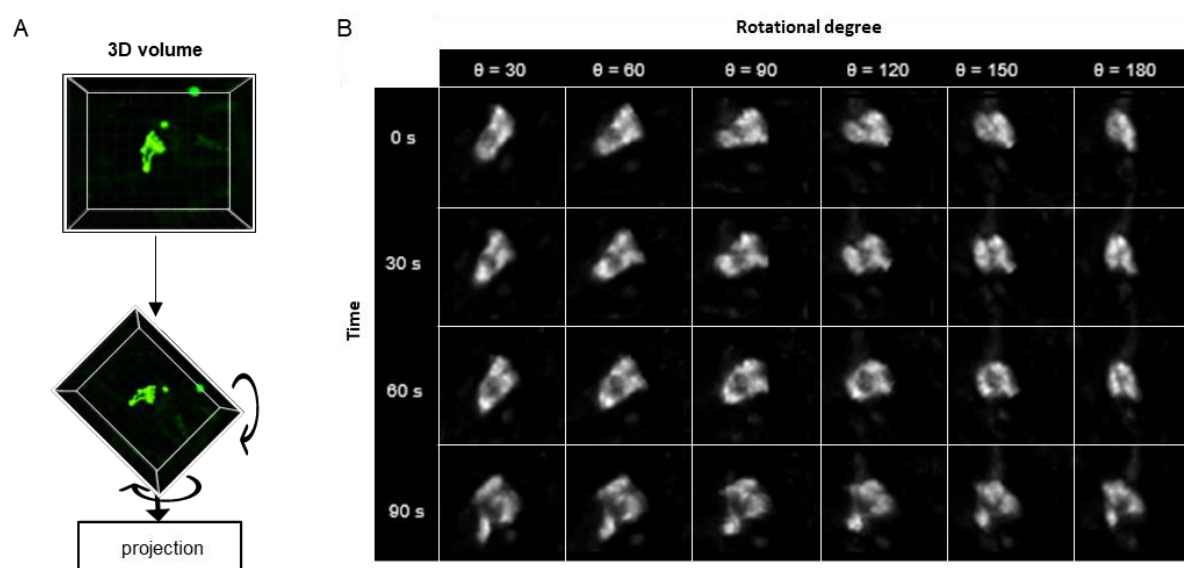
887 **Figure 5. 3D rotation of the** in vivo **dataset. A** *Depiction of a 3D volume cropped around an apoptotic cell. Each*

888 *collected apoptotic sequence underwent multiple 3D rotation in randomly sampled directions. The rotated 3D*

889 *images were successively flattened in 2D.* **B.** *Gallery showing the result of multiple volume rotations applied to the*

890 *same apoptotic sequence. The vertical axis depicts the sequence over time, whereas the horizontal describes the*

891 *rotational degree applied to the volumes.*
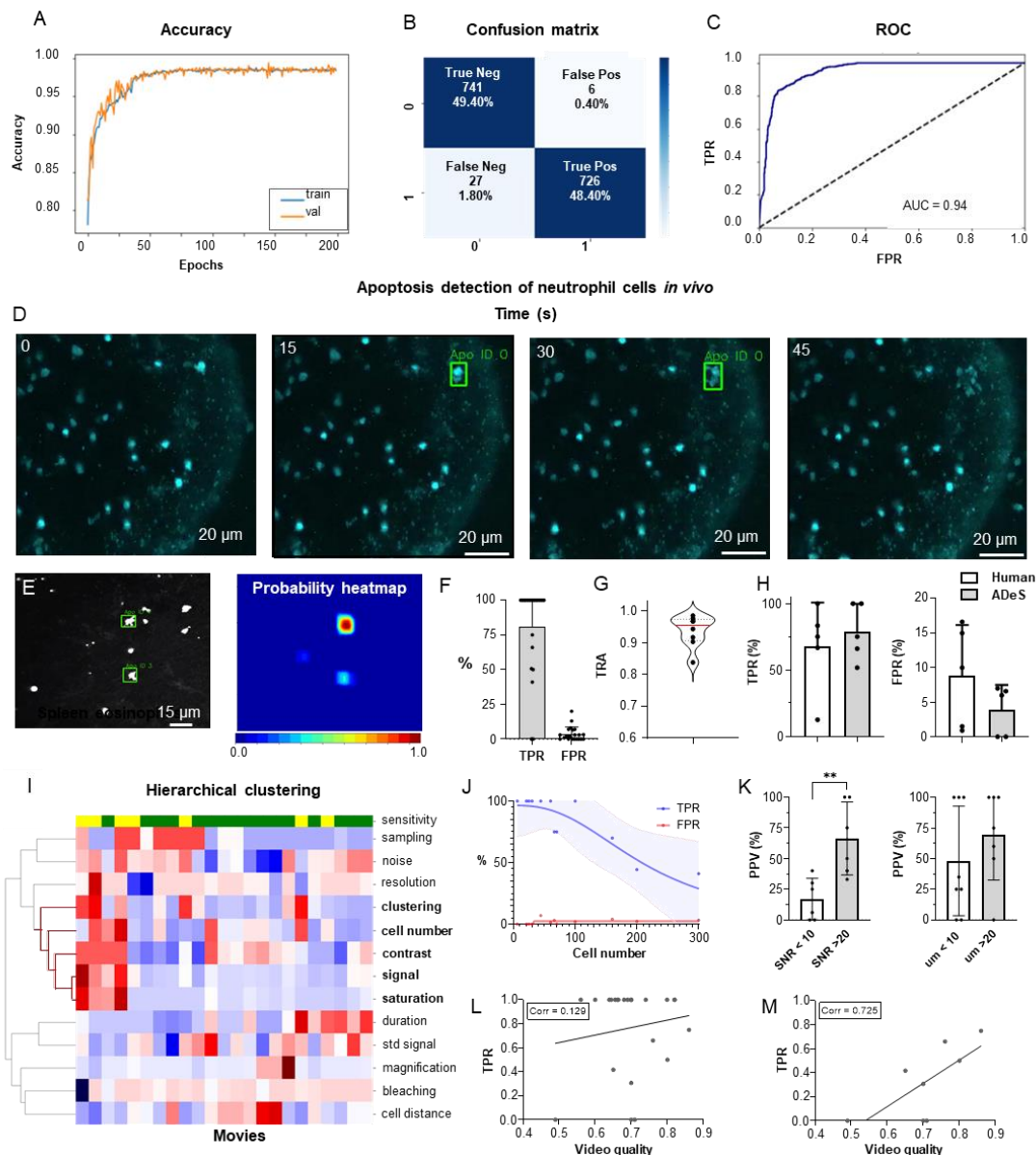
**Figure 6. Training and performance in vivo. A**. *Confusion matrix of the trained model at a decision-making threshold of 0.5.* **B**. *Receiver operating characteristic displaying the false positive rate (FPR) corresponding to each true positive rate (TPR).* **C**. *Training accuracy of the final model trained for 200 epochs with data augmentations.* **D**. *Image gallery showing ADeS classification to sequences with different disruption timing. The generated heatmap reaches peak activation (red) at the instant of cell disruption* **D**. *Representative snapshots of a neutrophil undergoing apoptosis. Green bounding boxes represents ADeS detection at the moment of cell disruption* **E**. *Representative micrograph depicting the detection of two eosinophil undergoing cell death in the spleen (**left**) and the respective probability heatmap (**right**).* **F**. *ADeS performances expressed by means of true-positive rate (TPR) and false-positive rate (FPR) over a panel of 23 videos.* **G**. *TRA measure distribution of the trajectories predicted by ADeS with respect to the annotated ground truth (n = 8)* **H**. *Comparison between human and ADeS by means of TPR and FPR on a panel of 5 randomly sampled videos* **I**. *Hierarchical clustering of several video parameters producing two main dendrograms (n = 23). The first dendrogram includes videos with reduced sensitivity and is enriched in several parameters related to cell density and signal intensity.* **J**. *Graph showing the effect of cell density on the performances expressed in terms of TPR and FPR (n = 13).* **K**. *Comparison of the positive predictive value*

908 *between videos with large and small signal to noise ratio (**left**), and videos with large and small shortest cell*

909 *distance (**right**). **L-M.** Selected video parameters are combined into a quality score that weakly correlates with the*

910 *TPR in overall data (**M, n = 23**) and strongly correlates with the TPR in selected underperforming data (**N, n = 8**).*

911 *Statistical comparison was performed with Mann-Whitney test. Columns and error bars represent the mean and*

912 *standard deviation respectively. Statistical significance is expressed as: $p \leq 0.05$ (*), $p \leq 0.01$ (**), $p \leq 0.001$ (***),*

913 *$p \leq 0.0001$ (****).*

914



915
916
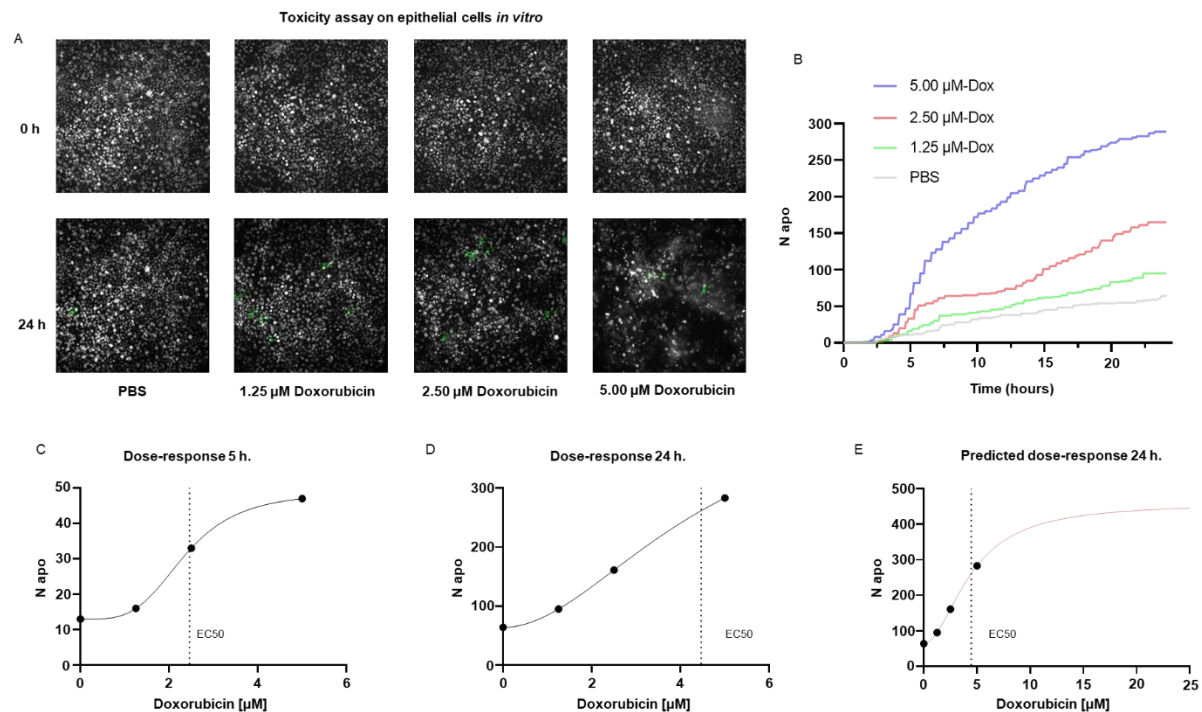
917 **Figure 7. Applications for toxicity assay** *in vitro*. **A**. *Representative snapshots depicting epithelial cells* in vitro

918 *at 0 and 24 hours after the addition of PBS and three increasing doses of doxorubicin, a chemotherapeutic drug*

919 *and apoptotic inducer* **B**. *Plot showing the number of apoptotic cells detected by ADeS over time for each*

920 *experimental condition.* **C-D**. *Dose-response curves generated from the drug concentrations and the respective*

921 *apoptotic counts at 5 h. and 24 h.post-treatment. Vertical dashed lines indicates the EC50 concentration.* **E**. *Dose-*

922 *response curve projected from the fit obtained in (**D**). The predicted curve allows to estimate the response at higher*

923 *drug concentrations than the tested ones.*

924
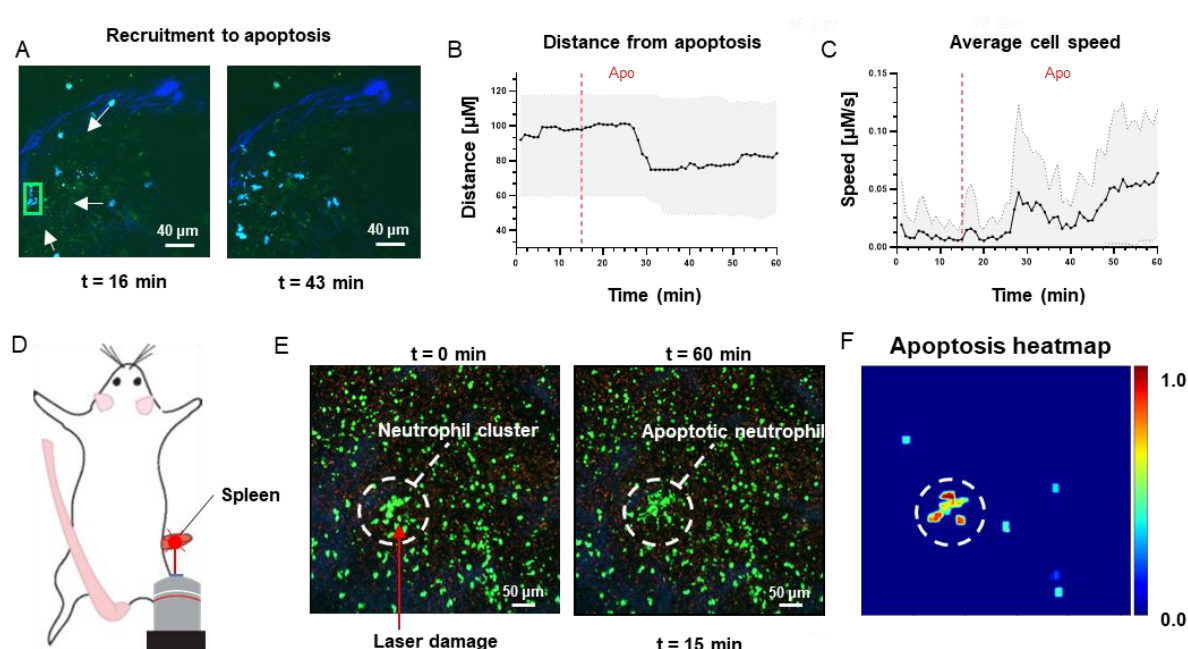
**Figure 8. Measurement of tissue dynamics** in vivo. **A**. Intravital 2-photon micrographs showing ADeS detection of an apoptotic neutrophil (Blue, left) and the subsequent recruitment of neighboring cells (right) in the popliteal LN at 19 h. following influenza vaccination. **B**. Plot showing the distance of recruited neutrophils with respect to the apoptotic coordinates over time ($n = 22$) **C**. Plot showing the instantaneous speed of recruited neutrophils over time ($n = 22$). The dashed vertical lines indicate the instant in which the apoptotic event occurs. **D**. Schematic drawing showing the intravital surgical set up of a murine spleen after inducing a local laser ablation. **E**. Intravital 2-photon micrographs showing the recruitment of GFP-expressing neutrophils (Green) and the formation of a neutrophil cluster (red arrows) at 60 min after photo burning induction. **F**. Application of ADeS to the generation of a spatiotemporal heatmap indicating the probability of encountering apoptotic events in the region affected by the laser damage. The dashed circle indicates a hot spot of apoptotic events.